

**1 Global 3-D electrical conductivity model of the world
2 ocean and marine sediments**

3 Alexander V. Grayver

4 Institute of Geophysics, ETH Zurich, Sonneggstrasse 5, 8092 Zurich, Switzerland

5 Key Points:

- 6 • New model of 3-D electrical conductivity of marine sediments**
- 7 • New 3-D electrical conductivity atlas of the world ocean with combined global and
8 regional data**
- 9 • Ocean and marine sediments have profound effect on electromagnetic responses
10 used for subsurface imaging and space weather impact evaluation**

11 **Abstract**

12 This study presents first global 3-D electrical conductivity models of the world ocean and
 13 marine sediments. Electrical conductivity of the ocean was calculated by invoking the
 14 Equation of State of Seawater (TEOS-10) with temperature and salinity data retrieved
 15 from the World Ocean Atlas and a series of high-resolution regional ocean climatology
 16 data sets. The resolution of the ocean conductivity atlas varies between 0.1° and 0.25°
 17 globally. The conductivity of marine sediments was estimated by using compaction and
 18 thermal gradient models constrained by real observations on a 5-arc-minute global
 19 marine sediment thickness grid. I present numerical simulations of electromagnetic induc-
 20 tion responses that demonstrate a significant effect of 3-D electrical conductivity of the
 21 ocean and marine sediments on electromagnetic responses for a broad range of frequen-
 22 cies. I show that both marine and land-based surveys designed for subsurface conduc-
 23 tivity imaging or Space Weather modelling will benefit from inclusion of more realistic
 24 conductivity models of the ocean and seabed sediments.

25 **1 Introduction**

26 The global ocean is a prominent electrical conductor with a relatively well-known
 27 geometry. The average vertical electrical conductance of the world ocean is approximately
 28 12,000 S with local values reaching up to 30,000 S. Additionally, due to penetration of
 29 the seawater and thermal gradients, marine sediments are typically very conductive. In
 30 some regions, the thickness of marine sediments can be more than 10 km (Straume et
 31 al., 2019) and the vertical conductance of marine sediments may exceed that of the over-
 32 lying ocean. As a result, the combined conductance of seawater and ocean sediments be-
 33 comes comparable to the conductance of the entire upper mantle (Heinson & Consta-
 34 ble, 1992; Utada et al., 2003; Baba et al., 2010; Grayver et al., 2017). As an example,
 35 the vertical conductance of the first 410 km in the global model by Grayver et al. (2017)
 36 is approximately 17,000 S, excluding water and sediment layers.

37 Ocean and sediments affect electromagnetic (EM) variations in a complex non-linear
 38 way across a wide range of frequencies. This effect is due to: (i) geometry of the seabed
 39 (and sedimentary layer where appropriate) and (ii) variability of electrical conductiv-
 40 ity within the ocean and sediments. The former has long been recognized as an impor-
 41 tant factor in EM induction modelling (Parkinson & Jones, 1979; Kuvshinov, 2008; Key
 42 & Constable, 2011), whereas the latter is poorly covered in the existing literature. Sub-
 43 surface conductivity distribution inferred from time-varying electromagnetic fields ob-
 44 served near the coast, within or above the ocean will be inaccurate if these two effects
 45 are not properly accounted for. Additionally, presence of large lateral conductivity con-
 46 trasts, such as between continents and oceans, can lead to strong geomagnetically induced
 47 currents (GICs) (Olsen & Kuvshinov, 2004; Kelbert, 2020). Therefore, accurate repre-
 48 sentation of conductivity gradients is important for accurate evaluation of space weather
 49 impacts on infrastructure.

50 The practical treatment of the ocean and sediments in EM induction studies may
 51 vary depending on the scale and survey design. For small-scale controlled-source EM (CSEM)
 52 and magnetotelluric (MT) marine surveys, local depth profiles of seawater conductiv-
 53 ity are often measured and this information can then be included in models. Some stud-
 54 ies showed that inverting for the seawater conductivity along with subsurface conduc-
 55 tivity can reduce model artifacts (Key, 2009). Both of these approaches are difficult to
 56 scale to 2-D and especially 3-D settings. Sometimes, dedicated survey designs may al-
 57 low for this (Attias et al., 2021), reporting improved convergence and discovering an or-
 58 der of magnitude variability in seawater conductivity. Nevertheless, for the vast major-
 59 ity of CSEM and MT studies, a uniform fixed seawater conductivity remains the most
 60 common assumption. The necessity to model ocean and marine sediments accurately is
 61 not a "curse" of marine surveys only. Land surveys carried near the coast will also be

62 affected by the ocean and marine sediments and one can find numerous studies that re-
 63 port difficulties in fitting data from coastal stations, not least because of a too simplis-
 64 tic representation of the ocean and the neglected EM induction effect due to marine sed-
 65 iments.

66 For large-scale and global EM induction studies, longer (more than few hours) pe-
 67 riods of natural EM variations are typically used. In these settings, induction effect due
 68 to conductive layers with thicknesses that are much less than the skin depth (such as the
 69 ocean and seabed sediments) is well approximated by a thin layer with an equivalent con-
 70 ductance. Therefore, it is common to represent ocean using a thin layer with laterally
 71 variable conductance (Kuvshinov, 2012; Kelbert et al., 2014). A uniform seawater con-
 72 ductivity has been typically assumed when deriving global conductance maps. Addition-
 73 ally, it is common to include conductance of marine sediments by assigning some con-
 74 stant conductivity values to marine sediments (Everett et al., 2003; Alekseev et al., 2015).

75 We note here that variability in seawater conductivity within the world ocean has
 76 received much more attention in studies where electrical current sources are generated
 77 by oceanic tides or other ocean current systems (Manoj et al., 2006; Minami, 2017; Velímský
 78 et al., 2018; Saynisch et al., 2017). In these settings, the current density, \vec{J} , within the
 79 water column is given by (in frequency domain) (Larsen, 1968; Chave & Luther, 1990;
 80 Tyler et al., 1997)

$$\vec{J} = \sigma(\vec{E} + \vec{u} \times \vec{B}), \quad (1)$$

81 where σ is the electrical conductivity of seawater, \vec{E}, \vec{B} are electric and magnetic fields,
 82 \vec{u} is the fluid velocity. We see that, unlike in other conventional EM induction methods,
 83 seawater conductivity here is scaled not only by the electric field (forming the con-
 84 duction current term, $\sigma\vec{E}$), but also by the motionally induced currents due to non-zero \vec{u}
 85 within the water column. Recent studies showed that spatiotemporal variations in the
 86 ocean conductivity result in small but potentially measurable effects in EM fields induced
 87 by oceanic currents (Velímský et al., 2019; Saynisch et al., 2017; Minami, 2017). In this
 88 context, Tyler et al. (2017) published a global 3-D conductivity distribution in the ocean
 89 at a lateral resolution of 1° by using the World Ocean Database (T. P. Boyer et al., 2013),
 90 which was recently updated by Reagan et al. (2019).

91 Table 1 provides a summary of open data sets on electrical conductivity of the ocean
 92 and marine sediments in relation to this work. One observation is that while ocean con-
 93 ductivity has received some attention, the electrical conductivity of marine sediments
 94 has at best been accounted for by assuming arbitrary constant conductivity values. As
 95 will be shown below, modern data allows us to estimate 3-D electrical conductivity of
 96 global marine sediments.

97 Another novelty of the present model is the usage of regional climatological data
 98 sets for estimation of the ocean electrical conductivity. Regional grids have higher res-
 99 olution compared to the global grids. As we shall see later, the improved resolution is
 100 particularly important when working in coastal areas.

101 2 Data and Methods

102 2.1 Bathymetry

103 The geometry of the seabed is relatively well known. Open data products such as
 104 GEBCO (Weatherall et al., 2015) and ETOPO1 (Amante & Eakins, 2009) provide global
 105 bathymetry grids at the 15-arc second and 1-arc minute resolutions, respectively. Higher
 106 resolution regional models are also widely available. Since we are mainly limited in res-
 107 olution by the ocean climatology data, 1-arc minute ETOPO1 grid will be used in this
 108 study (Figure 1).

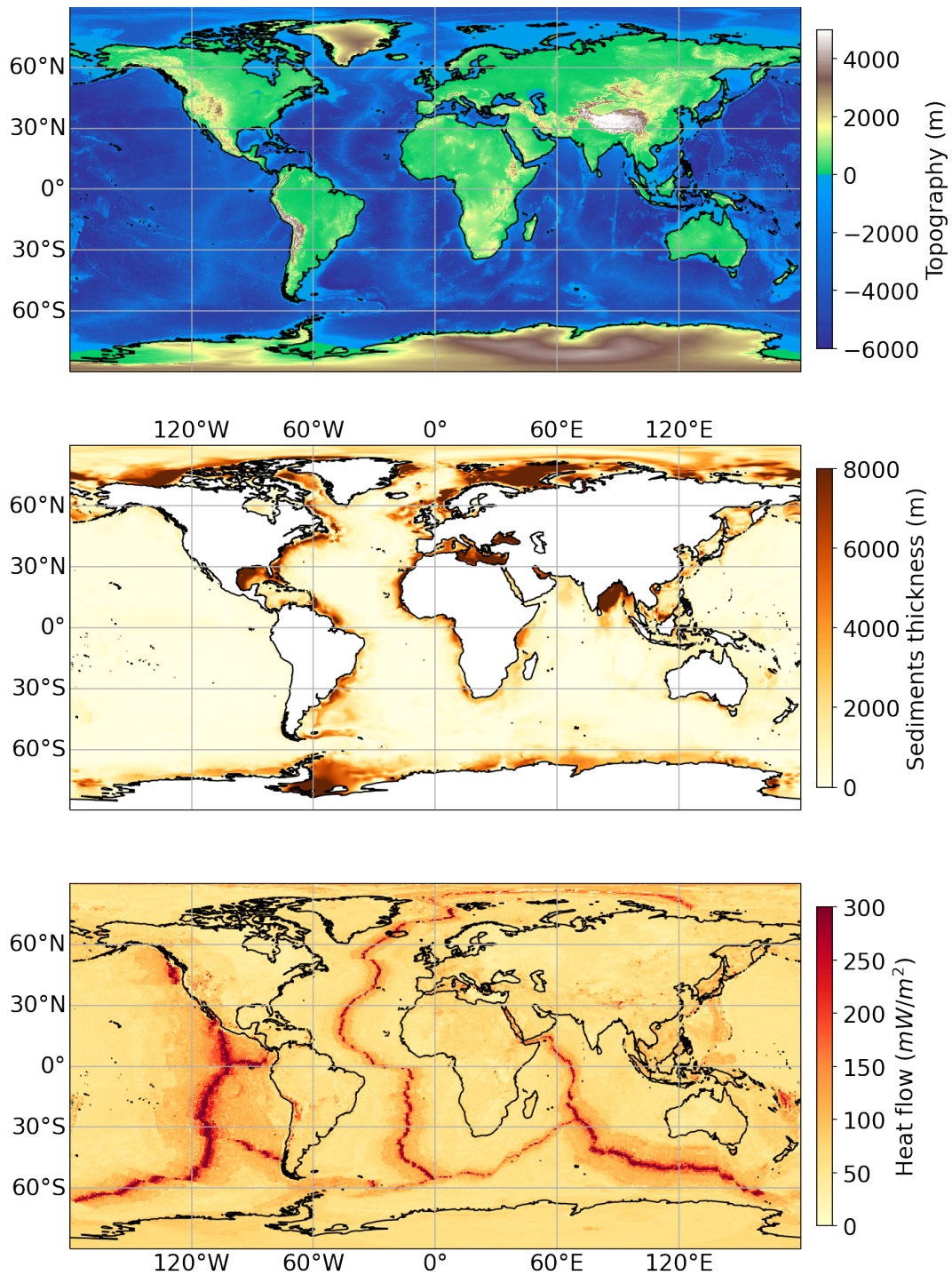


Figure 1. Input data used for construction of conductivity models. Top: ETOPO1 topography (Amante & Eakins, 2009); Middle: GlobSed (Straume et al., 2019) marine sediment thickness; Bottom: heat flow (Lucaleau, 2019) maps.

Table 1. Open data sets of electrical conductivity of the ocean and marine sediments. "N/A" stands for not available.

Source	Lateral resolution	Ocean conductivity	Sediment lateral resolution	Sediment conductivity
This study	0.1°-0.25°	3-D ¹	5'' ²	3-D
Reagan et al. (2019)	0.25°	3-D ³	N/A	N/A
Tyler et al. (2017)	1°	3-D ⁴	N/A	N/A
Grayver et al. (2016)	1°	2-D ⁵	N/A	N/A
Alekseev et al. (2015)	0.25°	Uniform $\sigma = 3.0 \text{ S/m}$	1° ⁶	0.5 S/m (water depth $\leq 500\text{m}$) 0.7 S/m (water depth $> 500\text{m}$)
Everett et al. (2003)	1°	Uniform $\sigma = 3.2 \text{ S/m}$	1° ⁶	0.8 S/m $\leq 7000 \text{ m.b.s.l.}$ 0.02 S/m $> 7000 \text{ m.b.s.l.}^7$

¹ See Table 2 for more information on data sources,

² GlodSed 5-arc-minute grid by Straume et al. (2019),

³ World Ocean Database 2018 (T. P. Boyer et al., 2013),

⁴ World Ocean Database 2013 (T. P. Boyer et al., 2013),

⁵ Depth-averaged conductivity based on World Ocean Atlas 2013 (Locarnini et al., 2013; Zweng et al., 2013),

⁶ Laske (1997)

⁷ "m.b.s.l." stands for metres below sea level.

109 2.2 Electrical conductivity of the ocean

110 Electrical conductivity of seawater is primarily controlled by temperature, salinity
 111 and pressure (Trossman & Tyler, 2019). These variables were used here to calculate
 112 seawater conductivity by invoking the Thermodynamic Equation of State for seawater,
 113 TEOS-10 (Feistel, 2008; Millero, 2010), through the Gibbs SeaWater (GSW) toolbox (McDougall
 114 & Barker, 2011). More specifically, electrical conductivity of seawater, σ_{sw} , is defined
 115 here as

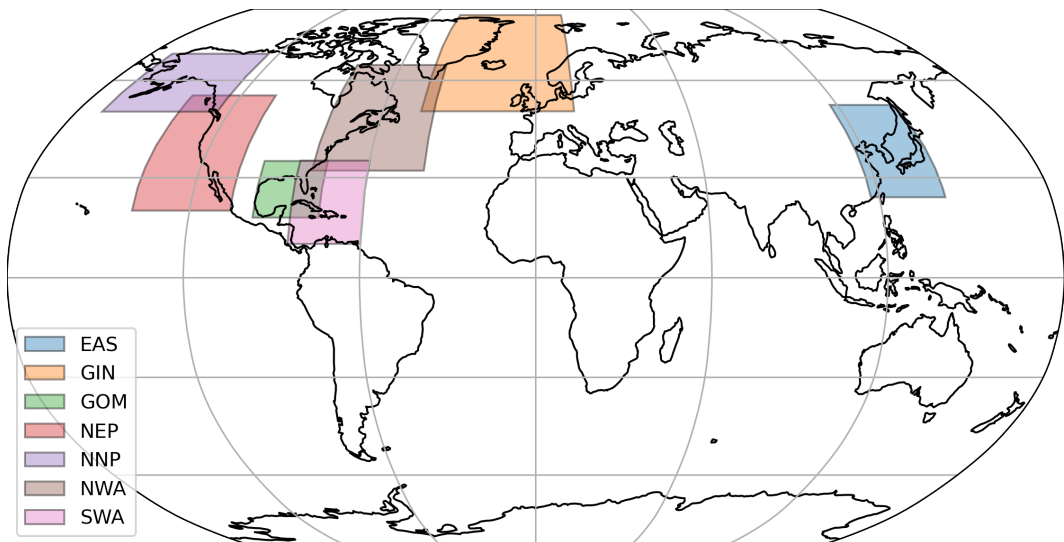
$$\sigma_{sw}(\vec{r}) \equiv \sigma_{TEOS}(T(\vec{r}), S(\vec{r}), P(\vec{r})), \quad (2)$$

116 where T, S, P denote temperature, salinity and pressure, all being functions of space. The
 117 vector $\vec{r} = (r, \theta_{GG}, \varphi_{GG})$ denotes a position with elements being distance from the origin,
 118 geographic co-latitude and longitude.

119 To get information on T and S , ocean climatology data listed in Table 2 were used
 120 in this study. The global quarter-degree grid was taken from the World Ocean Atlas 2018
 121 (WOA18) (Zweng et al., 2018; Locarnini et al., 2018). A number of regional climatolo-
 122 gies with the 0.1° resolution were added. In all cases, we used objectively analyzed cli-
 123 matology as defined in T. P. Boyer et al. (2013). The standard depth levels of WOA18
 124 were used, which cover water depths down to 5500 m with 102 layers ranging in thick-
 125 ness from 5 m at the sea surface to 100 m in deep ocean. For deeper waters, the values
 126 at 5500 m were assumed. When retrieving conductivity, regional climatologies are given

Table 2. Data sets of the ocean climatology used in this study.

Source	Area description	Acronym
Zweng et al. (2018); Locarnini et al. (2018)	Global	WOA18
Seidov et al. (2019)	The Southwest North Atlantic	SWA
Seidov et al. (2017)	The Northeast Pacific	NEP
Seidov, Baranova, Boyer, et al. (2016)	The Northern North Pacific	NNP
Seidov, Baranova, Johnson, et al. (2016)	The Northwest Atlantic	NWA
Johnson and Boyer (2015)	East Asian Seas	EAS
Seidov et al. (2018)	Greenland-Iceland-Norwegian Seas	GIN
T. Boyer et al. (2011)	The Gulf of Mexico	GOM

**Figure 2.** Map showing the coverage provided by high resolution regional climatological data sets. See Table 2 for area designations.

a higher priority due to higher resolution. Figure 2 shows the coverage of regional climatological data sets. As can be seen, these regional data sets are mostly around continental coasts where higher resolution is particularly important due to a complex shoreline.

The WOA18 and regional data sets provide monthly, seasonal and annual climatologies. Temporal variability in salinity and temperature will naturally result in different electrical conductivity values. As will be shown in Section 3.1, these changes are concentrated in the top 100 m of the water column and typically do not exceed a few per cent relative to the annual mean. Thus, using annual mean climatology is justified for conventional EM induction studies. However, if one works in shallow waters and regions where seasonal variability is expected to be high, considering electrical conductivity that

138 is based on a seasonal climatology may be justified. Results presented in this paper will
 139 be based on annual mean values averaged over decades (the exact time-span varies for
 140 different data sets, but covers at least one decade).

141 Note that the World Ocean Atlas is derived from the World Ocean Database (WOD),
 142 which, among other variables, provides profiles of salinity and temperature measured glob-
 143 ally at scattered locations. An alternative way to derive conductivity is to convert tem-
 144 perature and salinity data from the WOD to conductivity and then interpolate onto a
 145 regular grid. This approach was adopted in Tyler et al. (2017); Reagan et al. (2019) to
 146 derived global conductivity grids. As described in the references, this approach involves
 147 sophisticated data selection and is more cumbersome compared to the direct conversion
 148 of temperature and salinity grids performed in this study. Although the former approach
 149 is claimed to be more holistic, the resulting differences in conductivity values derived with
 150 two methods are generally small (on the order of a few per cent) and will play little role
 151 for most EM induction applications aimed at subsurface imaging or GICs modelling. How-
 152 ever, both data sets are openly available and a user should make an informed decision
 153 depending on their application and area of interest.

154 2.3 Electrical conductivity of marine sediments

155 For this study, information on the seabed sediment thickness was retrieved from
 156 the GlobSed (Straume et al., 2019) – a recent data-constrained global 5-arc-minute grid
 157 of total sediment thickness (Figure 1). For large-scale studies where sedimentary layer
 158 cannot be well resolved, it is advantageous to incorporate prior information on the con-
 159 ductance of the sedimentary column into modelling and inversion. However, unlike sea-
 160 water, electrical conductivity, σ_m , of marine sediments is generally not known and most
 161 studies either neglected it or assumed some constant values for the entire column (see
 162 Table 1). In this study, a data-driven model where conductivity of marine sediments varies
 163 laterally and with depth will be constructed.

164 Since marine sediments represent a porous medium saturated with a more electri-
 165 cally conductive fluid, their electrical conductivity is well approximated by the Archie's
 166 relationship (Archie, 1942)

$$\sigma_m(\vec{r}) = \sigma_f(\vec{r})\phi(\vec{r})^\beta, \quad (3)$$

167 where ϕ is porosity and σ_f pore fluid conductivity (hereinafter, we assume that $\sigma_f =$
 168 σ_{sw}). Vector \vec{r} denotes dependence of variables on all three coordinates, which vary lat-
 169 erally and radially. The exponent β , called formation factor, depends on a rock, but typ-
 170 ically lies between 1.5 and 2.5 for sedimentary basins (Jackson et al., 1978; Evans, 1994;
 171 Breitzke, 2006; Glover, 2016). Although β should also be a function of space, we ignored
 172 this complication here and used a fixed value of $\beta = 2$ that is common in the litera-
 173 ture.

174 Porosity will generally exhibit decreasing trend with depth as a result of compaction
 175 (Velde, 1996; Bahr et al., 2001; Revil et al., 2002; Martin & Wood, 2017). In its simplest
 176 form (known as Athy's model), porosity decays exponentially with depth (Hantschel &
 177 Kauerauf, 2009; Wallmann et al., 2012):

$$\phi(z) = \phi_0 e^{-c_0 z}, \quad (4)$$

178 where ϕ_0 is the porosity at the sediment-water interface (SWI), c_0 (m^{-1}) denotes the
 179 compaction length-scale and z (m) is depth from the Earth's surface. Note the relation
 180 $z = a - r$, where a is the radius of a planet. Deep drilling experiments confirm that
 181 eq. (6) is a reasonable model for marine sediments down to depths of at least 5 km (Velde,
 182 1996). The disadvantage of this simple model is that it permits arbitrarily small poros-
 183 ity values, sometimes leading to non-physical behaviour (Bahr et al., 2001; Hantschel &
 184 Kauerauf, 2009). To avoid this, a non-zero minimum porosity value, ϕ_{min} , can be incor-

185 porated into eq. (6) yielding

$$\phi(z) = \phi_{min} + (\phi_0 - \phi_{min})e^{-c_0 z}. \quad (5)$$

186 The value of ϕ_{min} will depend on the grain type. For deep marine sediments, minimum
187 porosity of approximately 5 per cent was observed (Velde, 1996). Therefore, we used a
188 fixed value of $\phi_{min} = 0.05$ in this study.

189 Decrease in electrical conductivity of sediments with depth associated with reduced
190 porosity will be counteracted by the increase in the ambient temperature, which will en-
191 hance conductivity of the pore fluid. In this study, the steady-state temperature profile
192 of marine sediments was calculated as (Wallmann et al., 2012)

$$T_{sed}(z) = T_{SWI} + z \frac{q}{\lambda_{sed}^{1-\phi(z)} \cdot \lambda_f^{\phi(z)}}, \quad (6)$$

193 where T_{SWI} (K) stands for temperature at the SWI, q is the heat flow (W/m^2), $\lambda_f \approx$
194 0.6 (W/mK) and λ_{sed} are thermal conductivities of the seawater and sediments, respec-
195 tively. T_{SWI} was extracted from the WOA18 and regional climatologies (see Section 2.2),
196 heat flow model from Lucaleau (2019) was used to define q (see Figure 1).

197 Parameters ϕ_0 , c_0 and λ_{sed} depend on a sediment rock type. In this work, we de-
198 fined three regions of the ocean bottom (LaRowe et al., 2017): shelf (0-200 m.b.s.l.), mar-
199 gins (200-3500 m.b.s.l.) and abyssal domains (> 3500 m.b.s.l.). The actual values for all
200 variables are listed in Table 3.

Table 3. Physical properties of global marine sediments used to define the porosity and thermal gradient models.

Parameter	Shelf ¹	Margin ²	Abyss ³
ϕ_0	0.55	0.63	0.7
c_0	5e-4	5.7e-4	8.3e-4
λ_0	2.7	2.5	1.7

¹ Values representative of a sandstone-silt-shale mixture (Hantschel & Kauerauf, 2009),

² Grevemeyer and Villinger (2001)

³ Typical shale (Hantschel & Kauerauf, 2009)

201 Estimated temperatures T_{sed} are used to calculate σ_f using the equation of state
202 of seawater TEOS-10 (Millero, 2010). However, TEOS-10 was only calibrated for $T \leq$
203 80°C (Feistel, 2008), whereas in deep sedimentary basins, T_{sed} can easily exceed this value.
204 Carried tests showed that conductivity values inferred from the TEOS-10 for $T > 80^\circ\text{C}$
205 are inaccurate. Therefore, at $T > 80^\circ\text{C}$ conductivity values were linearly extrapolated.

206 We also note here that some studies used conductivity models of NaCl solution
207 in pure water to calculate pore fluid conductivity in marine sediments and shallow crust.
208 Although high-quality electrical conductivity models of $\text{H}_2\text{O}-\text{NaCl}$ solution exist (Guo
209 & Keppler, 2019; Simmyo & Keppler, 2017), they shall not be used as a substitute for
210 electrical conductivity of seawater in sediments because: (i) they may not fully cover the
211 relevant range of $P-T$ values in sediments, and (ii) small fractions of other salts in sea-
212 water (in particular, Mg and Ca) significantly enhance conductivity. As an example, for
213 $T = 80^\circ$, average ocean salinity of 3.5% and $P = 10$ dbar, the empirical relation of

214 Sinmyo and Keppler (2017) predicts $\sigma_{NaCl} = 6.18$ S/m, whereas TEOS-10 yields $\sigma_{sw} =$
215 11.46 S/m for the same conditions.

216 Finally, using compaction and thermal models described above and employing the
217 Archie's relation, we can estimate depth-dependent electrical conductivity of marine sedi-
218 ments. Note that additional complications related to heterogeneties in structure and com-
219 position within marine sediments will generally affect conductivity. Therefore, the de-
220 rived conductivity model is considered a general estimate by assimilating the available
221 observations and known principles, but remains an approximation due to the stated com-
222 plications. Nevertheless, the presented conductivity model of marine sediments is a sub-
223 stantial step forward compared to the present practice of either neglecting marine sedi-
224 ments or using arbitrary constant values to define their conductivity.

225 It is worth to explicitly mention here that the present conductivity model of ma-
226 rine sediments does not use the ocean conductivity as an input, making models derived
227 in Section 2.2 and in this section independent.

228 2.4 Averaged conductivity and conductance

229 In order to mitigate very high computational cost, 3-D heterogeneous ocean and
230 sediment layers can be approximated by thin spherical shells with equivalent vertical con-
231 ductance. This approximation is valid for large-scale EM induction studies that involve
232 long periods (more than few hours). At a given location with coordinates $(\theta'_{GG}, \varphi'_{GG})$
233 on the surface of Earth, the vertical conductance is given by

$$C(\theta'_{GG}, \varphi'_{GG}) = \int \sigma(\vec{r}') dr', \quad (7)$$

234 where $\vec{r}' = (\theta'_{GG}, \varphi'_{GG}, r')$ and integration is confined to the ocean or sediments layers.

235 In addition, we can define the depth-averaged conductivity as

$$\sigma_{avg}(\theta'_{GG}, \varphi'_{GG}) = \frac{C(\theta'_{GG}, \varphi'_{GG})}{\int dr'}, \quad (8)$$

236 3 Results

237 3.1 Ocean

238 Electrical conductivity of the ocean was calculated as described in Section 2.2. The
239 distribution of the salinity and temperature as well as resulting electrical conductivity
240 are shown in Figures 3 and 4 at the sea surface and at 200 m depth, respectively. Clear
241 correlations between the conductivity and climatological variables are evident that also
242 extend to depth. Because of the natural variability in latitude, it is insightful to also
243 look at these quantities in form of cross-sections, calculated by averaging the values with
244 respect to longitude (Figure 5). As is evident from these cross-sections, the major part
245 of the variability in electrical conductivity of the ocean is limited to the first 1 km at mid
246 and low latitudes, which in turn is linked to variations in climatological variables.

247 Additionally, Figure 6 shows seasonal variations by calculating the Winter and Sum-
248 mer electrical conductivity anomalies. The effect does not exceed 0.2 S/m in amplitude
249 relative to the annual mean and is limited to the shallowest 100 m at latitudes $\pm 60^\circ$ equa-
250 torward. Therefore, using electrical conductivity derived from the annual mean values
251 will suffice for the majority of EM induction studies.

252 As was already mentioned in the introduction, the electrical conductivity of the ocean
253 was presented and thoroughly analyzed in several studies (Tyler et al., 2017; Trossman
254 & Tyler, 2019; Saynisch et al., 2017; Minami, 2017). The reader interested in more de-

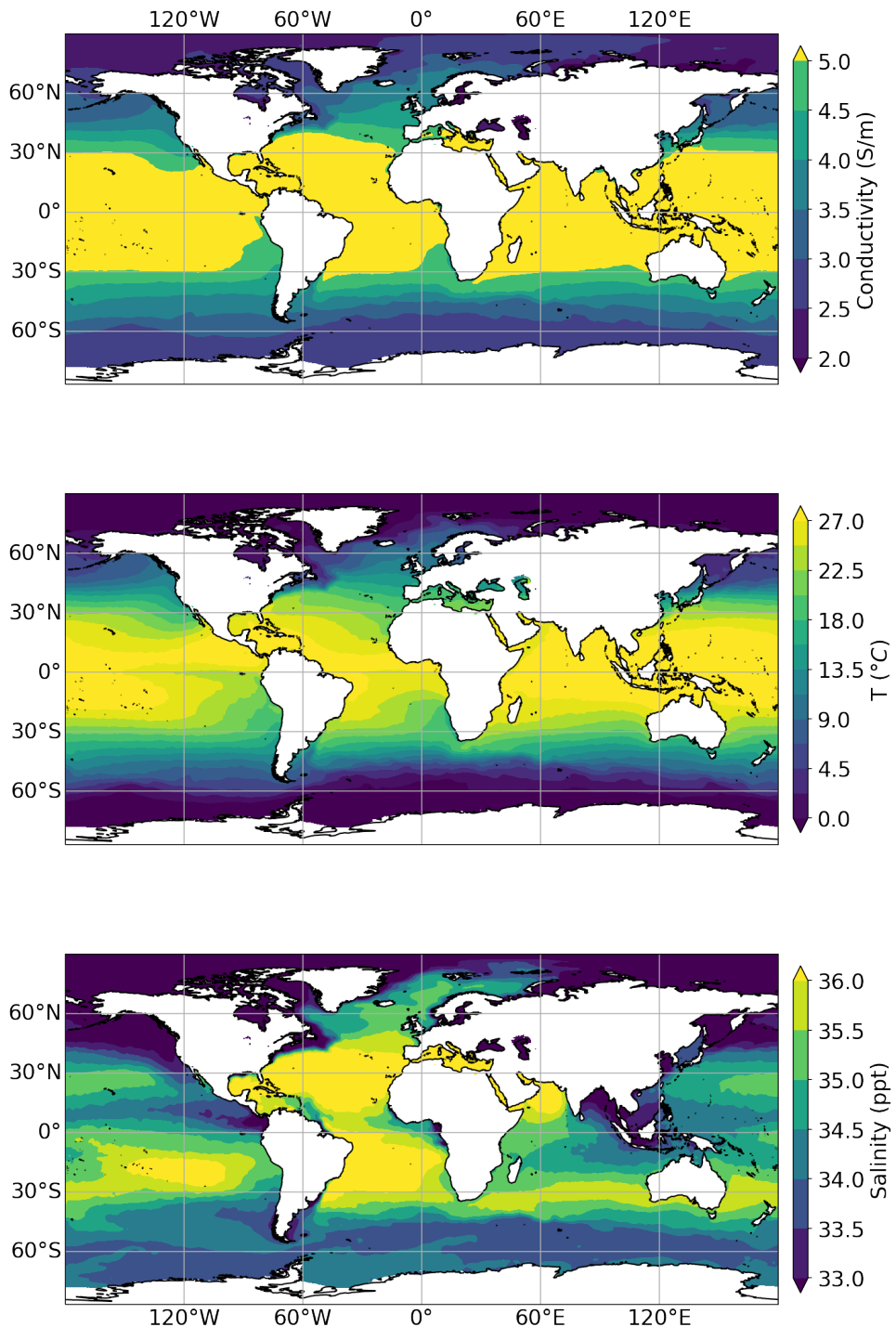


Figure 3. Maps of the ocean electrical conductivity, temperature and salinity at the sea surface.

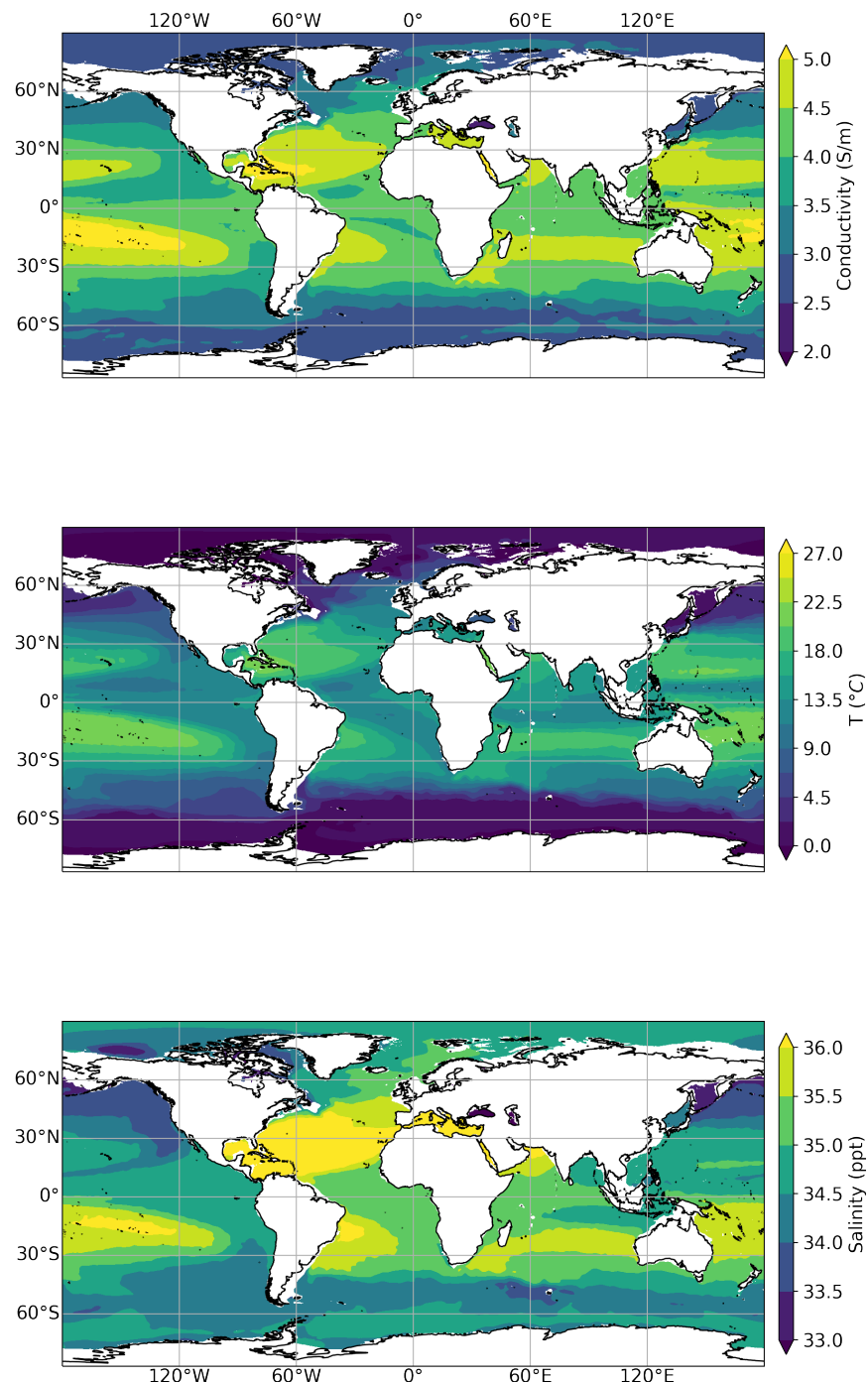


Figure 4. Same as Figure 3, but at 200 m below sea surface.

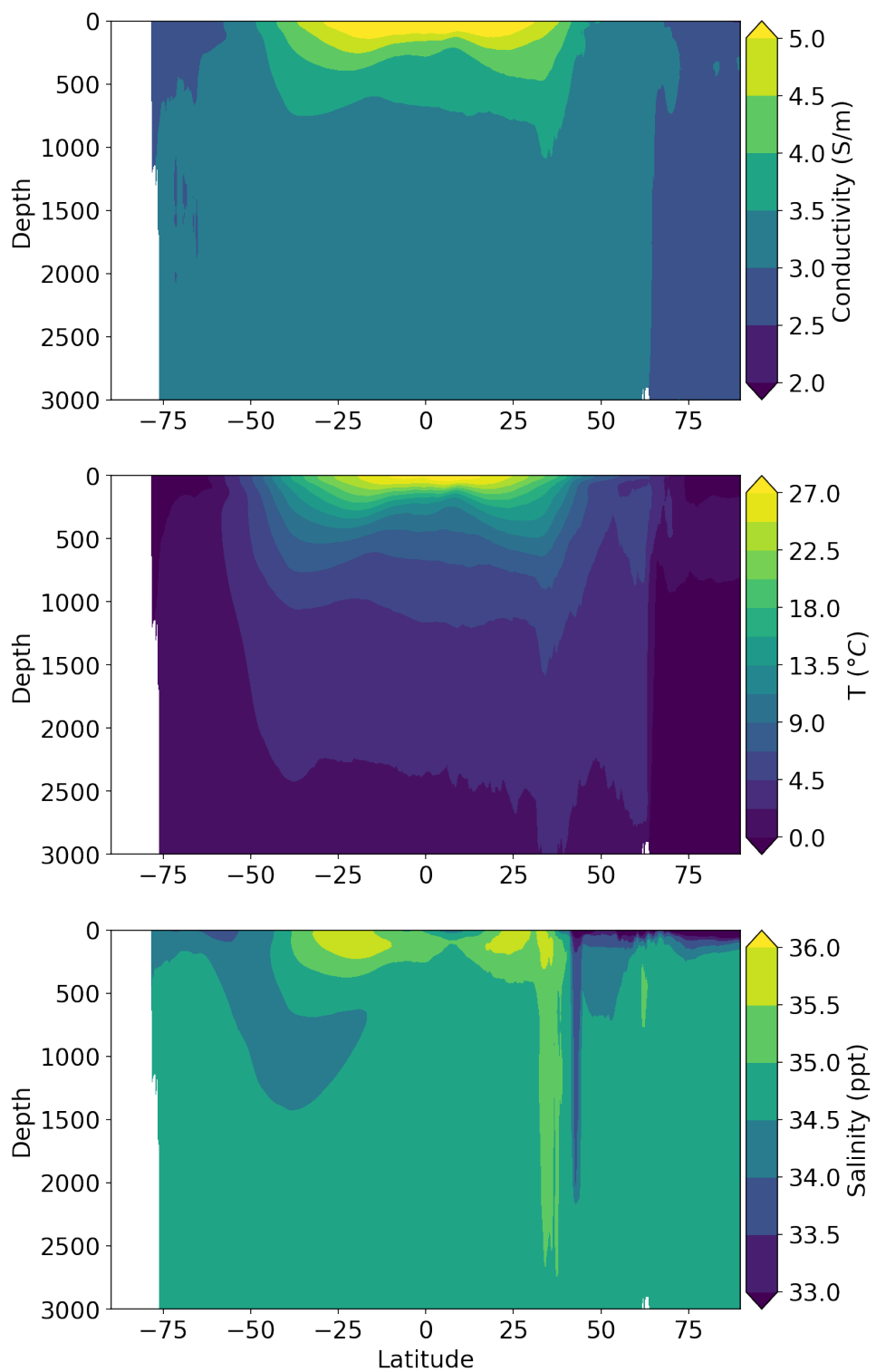


Figure 5. Cross sections of the electrical conductivity, temperature and salinity of the ocean averaged over all longitudes.

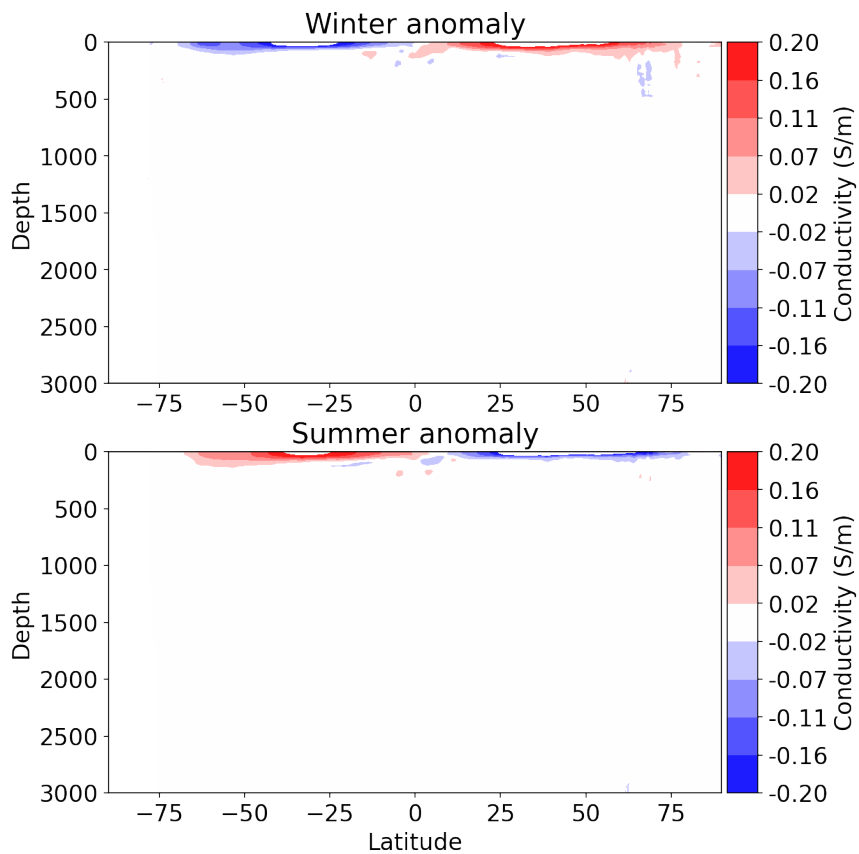


Figure 6. Cross sections of the winter and summer anomalies in the electrical conductivity relative to the annual mean (Figure 5), averaged over all longitudes.

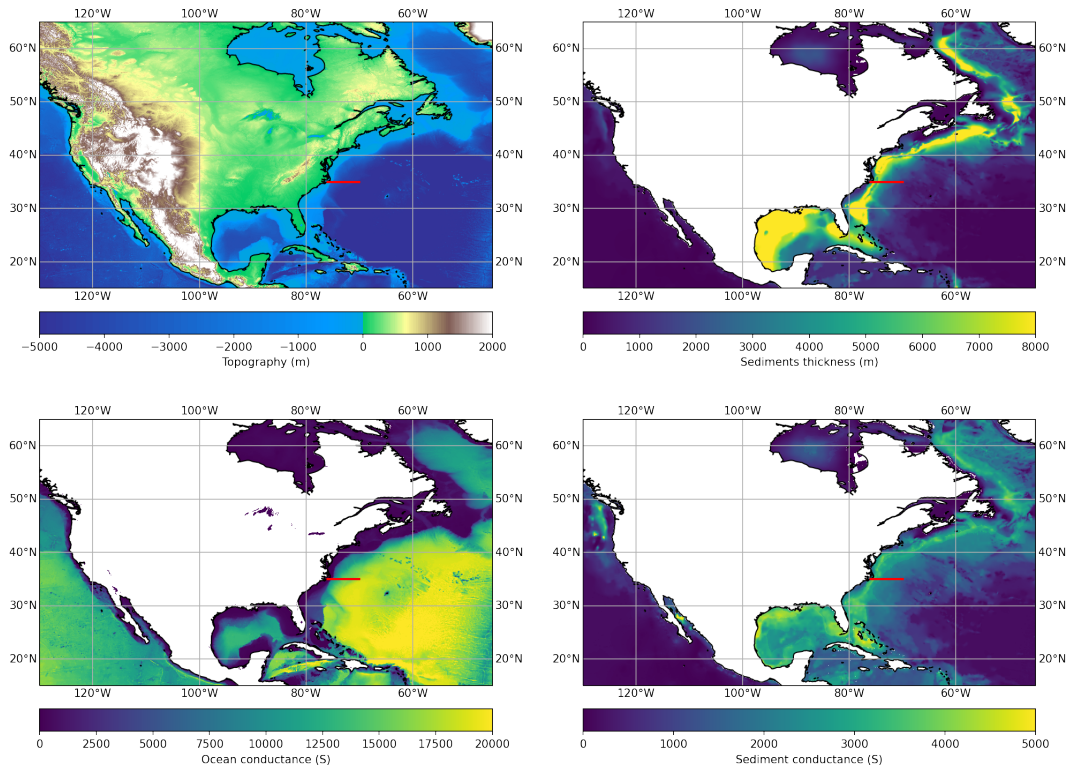


Figure 7. Top row: Maps of the elevation, marine sediment thickness. Bottom row: radial electrical conductance of the ocean and marine sediments. Red line shows the locations of the profile from Figure 8.

tails about ocean climatology and its effect on conductivity is referred to cited studies and references therein.

3.2 Marine sediments

The major contribution of this study is a new electrical conductivity model of marine sediments that is described in Section 2.3. In the next section, we will calculate and analyze the global conductance map of marine sediments based on the present model. In this section, we will look at the 3-D variations of the model for a specific location. Figure 7 shows the conductance maps of the ocean and marine sediments around the North America. A cross section at the east coast of the US shown in Figure 8 plots conductivity values within the ocean and sediments derived from our models. One can see the decrease in conductivity with depth within the ocean and some variability in the east-west direction. Much larger conductivity changes can be seen within the sediments. Variations due to porosity and temperature changes with depth are most evident. There are also lateral variations which are most pronounced when we go across sediment types.

Figure 9 shows depth profiles of conductivity and other quantities for the ocean and sediments at one location of the continental margin. One clearly sees how the decrease in the bulk conductivity associated with the reduced porosity is counteracted by increasing conductivity of the pore fluid that reaches values of ≈ 20 S/m at the depth of 8 km due to high temperatures.

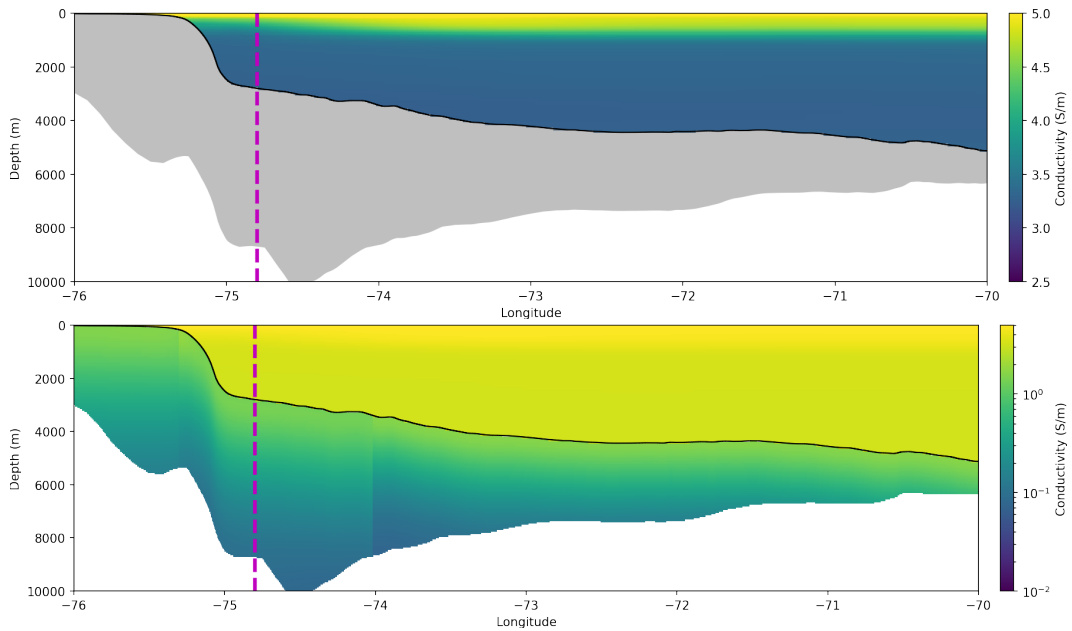


Figure 8. Electrical conductivity section along the red profile line shown in Figure 7. Top: electrical conductivity within the ocean (linear color scale). Bottom: section showing both ocean and sediments conductivity values (logarithmic color scale). Magenta dashed line shows the location for which the values shown in Figure 9 were plotted.

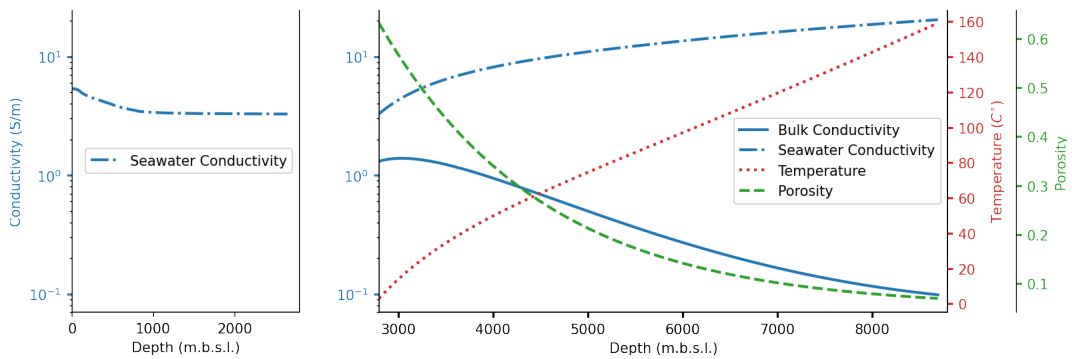


Figure 9. Depths profiles of the conductivity within the water column and sediments along with other relevant parameters for a location depicted in Figure 8. The exact coordinates of the point are 35°N, 74.8°W.

274 **3.3 Global conductance maps**

275 Global conductance maps of the ocean and marine sediments were calculated fol-
 276 lowing eq. (7). In order to avoid unrealistically low values for very shallow waters, we
 277 require the conductance of the water column to be at least 1 S. Without these adjust-
 278 ments, conductance values as small as 10^{-3} S were obtained at isolated grid points. Such
 279 outliers can have negative impact on numerical modelling and should be avoided.

280 Figure 10 shows global conductance maps of marine sediments and the world ocean.
 281 As anticipated, the conductance of the ocean is clearly dominated by the bathymetry.
 282 To highlight lateral variability pertained to the ocean itself, we additionally calculated
 283 the depth-averaged conductivity of the ocean (Figure 10). It is apparent that even af-
 284 ter averaging radial variability, assigning a constant conductivity to the ocean would be
 285 a rather crude approximation.

286 The conductance of marine sediments is also generally highly correlated with the
 287 sediment thickness (cf. Figures 1 and 10). However, a closer look also reveals spatial vari-
 288 ability related to the variations in sediment types and sea bottom heat flow. In addition
 289 to its spatial complexity, the conductance values also reveal that accounting for the ma-
 290 rine sediments in EM modelling studies is most important in the coastal areas.

291 Figure 11 depicts difference between the marine sediment conductance model de-
 292 rived in this work and the model constructed following Everett et al. (2003) (see Table
 293 1). Note systematic differences between the two maps: for regions with thick sediments,
 294 sediment conductance derived after Everett et al. (2003) exceeds our by as much as 2000
 295 S, whereas our model depicts larger conductance values in comparison for areas of low
 296 sediment thickness. This is expected since the approach of Everett et al. (2003) assigns
 297 a constant conductivity value of 0.8 S/m to the first 7 km. As Figure 9 shows, this value
 298 is often too low for sediments right at the SWI and too high for deep sediments where,
 299 due to the reduction in porosity, conductivity also quickly decreases to values less than
 300 0.8 S/m. For a normal geotherm and assuming the Archie's relation holds, electrical con-
 301 ductivity of 0.8 S/m at 7 km depth would require porosities of ≥ 0.2 , which is rather un-
 302 likely (Velde, 1996; Hantschel & Kauerauf, 2009).

303 **4 Effect on electromagnetic responses**

304 This section aims to demonstrate the effect of 3-D conductivity variations within
 305 the water column and sediments on EM induction responses. Ultimately, all the effort
 306 of constructing the models described above is only relevant if our data is sensitive to these
 307 conductivity variations. Owing to the complexity of the ocean and its non-linear effect
 308 on EM responses, it is hard to design tests that would cover all practical scenarios. Nev-
 309 ertheless, the examples considered below should be representative of many real studies.
 310 All EM responses shown in the following sections were calculated with the GoFEM finite-
 311 element code (Grayver & Kolev, 2015).

312 **4.1 Marine Magnetotellurics**

313 Our first example will consider a marine MT case. Marine EM responses are likely
 314 to be affected the most by the conductivity variations in seawater. Previous studies (Key
 315 & Constable, 2011; Worzezki et al., 2012) showed that bathymetry leads to severe dis-
 316 tortions in MT responses and should be modelled accurately. The goal here is to quan-
 317 tify the effect of the conductivity variations of seawater on marine MT responses in the
 318 presence of realistic bathymetry. To this end, we will look at a profile west of Mexico (Fig-
 319 ure 12). Due to undergoing subduction in this region, there is a complex bathymetry,
 320 while marine sediments are relatively thin, mostly within a few hundred meters. There-

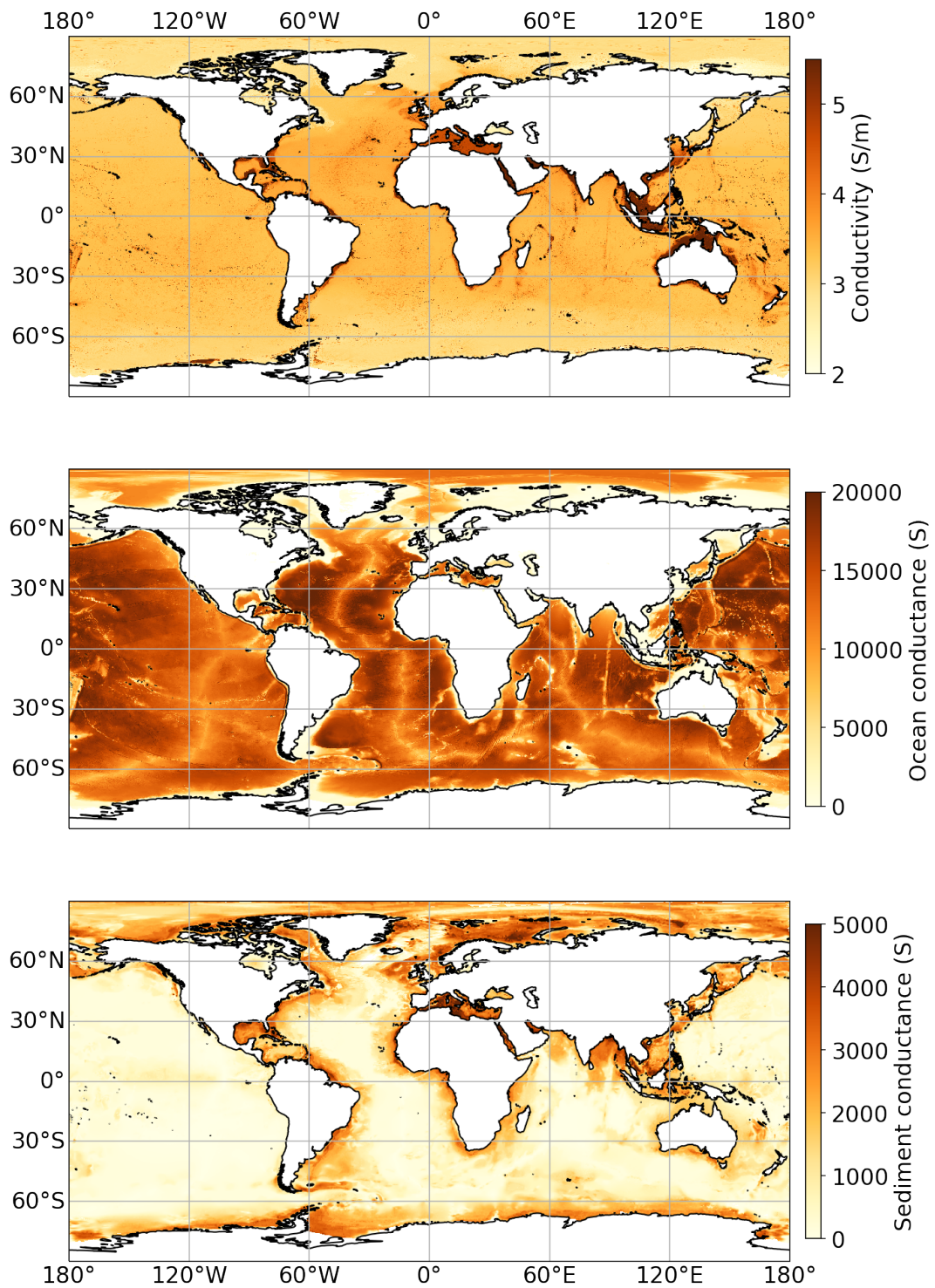


Figure 10. Depth-averaged conductivity of the ocean (top) and electrical conductance maps of the ocean (middle) and marine sediments (bottom). The shown quantities were derived as described in Section 2.4.

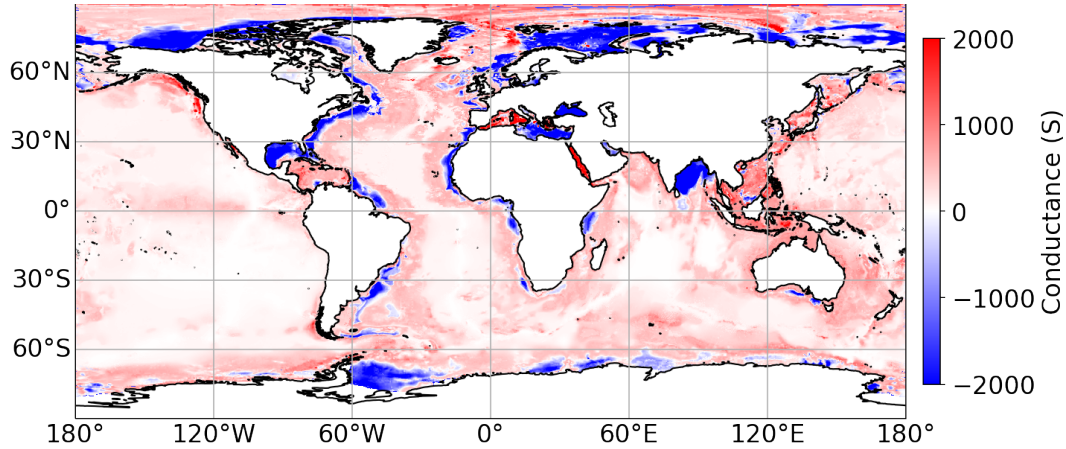


Figure 11. Difference in the electrical conductance of marine sediments calculated by using the model derived in this work and the one derived following Everett et al. (2003).

fore, this area is suitable for studying the effect of realistic ocean conductivity on MT transfer functions (TFs) in a dedicated manner.

The discrete 2-D conductivity model and distribution of stations are shown in Figure 13. Note that in addition to the sea bottom stations, we also placed some stations on land in order to see how far the effect of realistic ocean penetrates inland. We will test two models of the ocean: homogeneous ocean with the constant conductivity of 3.2 S/m and ocean with realistic conductivity (shown in Figure 13). Additionally, subsurface conductivity values of 0.1 and 0.02 S/m will be tested. We will calculate frequency-dependent plane-wave MT transfer functions, called impedance (Berdichevsky & Dmitriev, 2008). For a 2-D case, when conductivity is assumed to be constant in the x -direction, two transfer functions, referred to as TE and TM modes, are defined as

$$Z_{TE} = \frac{E_x}{H_y}, Z_{TM} = \frac{E_y}{H_x}. \quad (9)$$

All quantities in the equations above depend on frequency and location. We will display these quantities in form of apparent resistivity and phase, defined as

$$\rho_\alpha^{\text{app}} = \frac{|Z_\alpha|^2}{\omega\mu}, \varphi = \tan^{-1} \frac{\text{Im}Z_\alpha}{\text{Re}Z_\alpha}. \quad (10)$$

Figures 14-15 show pseudo-sections of the apparent resistivity and phase values calculated along the profile for two models with different conductivity values of the homogeneous subsurface (0.02 and 0.1 S/m). We see that the effect of seawater conductivity variations on MT responses becomes smaller as the conductivity contrast between water and ocean bottom decreases. The same is true also for the effect of bathymetry itself (Key & Constable, 2011). To assess the effect of realistic ocean conductivity, relative differences between transfer functions calculated with the homogeneous and 2-D ocean models are shown in Figures 16-17. They demonstrate that even for the low-contrast case, there are many stations and periods where differences would exceed typical error floor values used in inversions. In addition to marine stations that are the most affected by the variations in the ocean conductivity, the effect for inland stations is less significant, but still reaches $\approx 20\%$ at long periods.

Another observation revealed by this example is that the magnitude of the effect strongly depends on the bathymetry profile. First, there is a positive correlation between

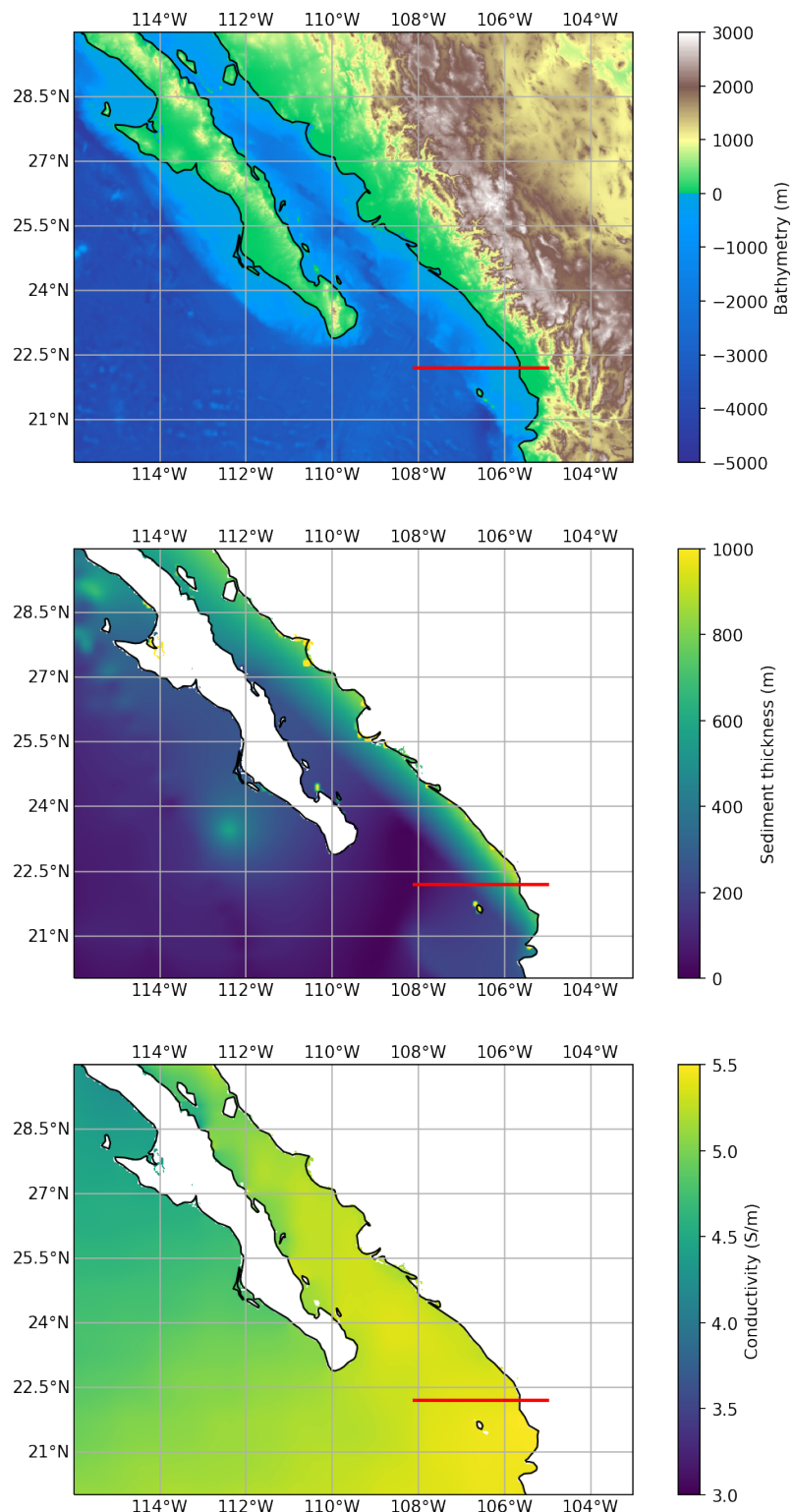


Figure 12. Maps showing topography, thickness of marine sediments and sea surface conductivity in the west of central America. Location of the profile is depicted with a red line.

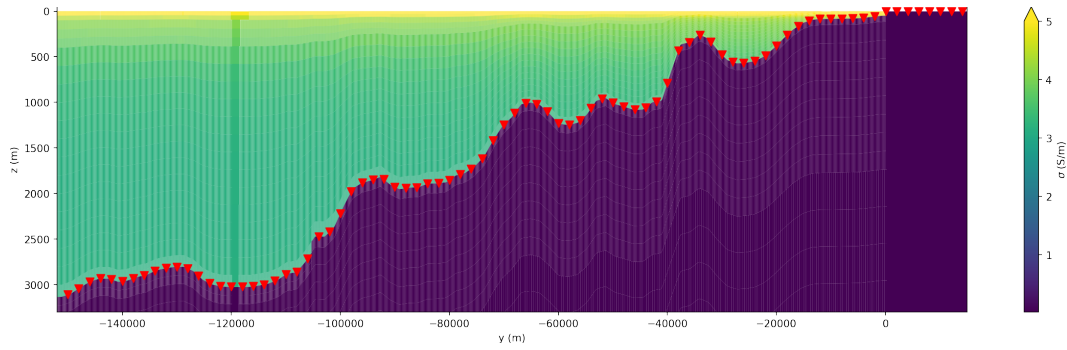


Figure 13. Discrete conductivity model constructed along the profile shown in Figure 12. Red triangles show location of stations. Conductivity of the ocean is based on the realistic ocean climatology (Section 2.2).

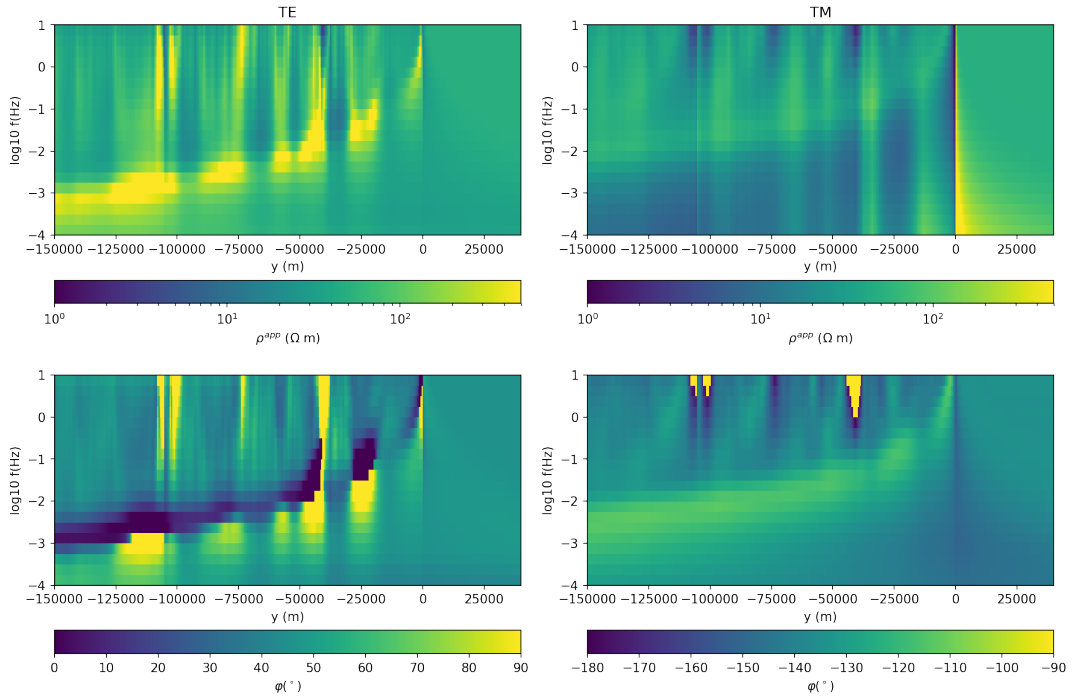


Figure 14. Cross sections of the MT transfer functions calculated for a model shown in Figure 13. The conductivity of 0.02 S/m was assigned to the subsurface. Left and right columns show apparent resistivity and phase values for the TE and TM modes, respectively.

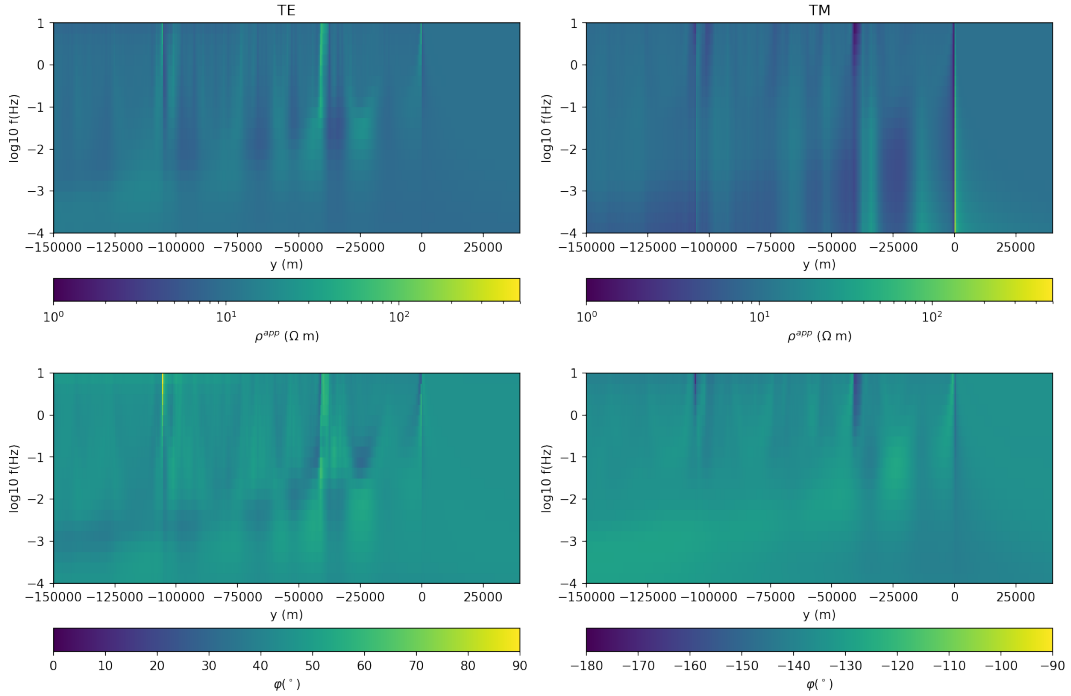


Figure 15. Same as Figure 14, but for a homogeneous subsurface conductivity of 0.1 S/m. Note the different color scale for the ρ^{app} .

the ocean depth and period at which the maximum effect in TFs is observed. Further, we see some strong effects, particularly in the TE mode, at stations located on or close to steep bathymetry slopes (for instance, at $y \approx -40$ km or $y \approx -105$ km). At these locations, the effect is significant across the whole simulated range of periods.

In this example we neglected marine sediments, which would typically be more conductive at the SWI than the 0.1 S/m value used in this example (Figures 15 and 17). One may argue that in the presence of very conductive marine sediments the effect due to realistic seawater conductivity distribution may fall below the error floor and using constant seawater conductivity would suffice, at least in areas with thick marine sediments. However, such simple reasoning may be misleading. Although conductivity contrast at SWI will indeed decrease due to conductive marine sediments, the magnitude of the induction effect due to heterogeneous seawater also depends on other factors, such as bathymetry profile and location of stations. Therefore, each survey would demand a dedicated modelling study to assess if the constant seawater conductivity would suffice. Another argument in favor of using more realistic seawater conductivity distribution is the fact that one usually performs inversion by starting from a simple (often homogeneous) conductivity model that does not include sediment layer and is usually more resistive than marine sediments at SWI. In this case, using some constant average value for the entire seawater column may result in subsurface artifacts or facilitate entrapment in a local minimum (Wheelock et al., 2015).

4.2 Land Magnetotellurics

It is generally accepted that land-based EM measurements taken in the vicinity of the ocean need to account for the ocean EM induction effect. The most common way to do this is to incorporate some representation of the ocean into a model. However, as a result of thick sediments and/or large thermal gradients, the conductance of marine

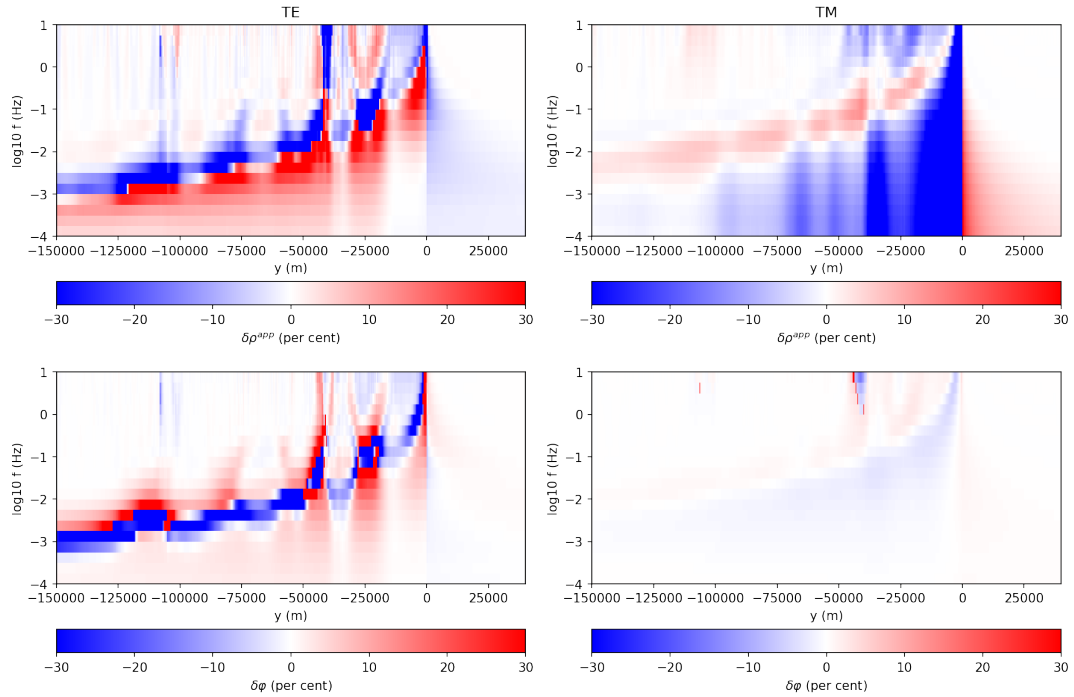


Figure 16. Cross sections of the relative differences between transfer functions calculated using a climatology-constrained ocean conductivity (Figures 13–14) and a homogeneous ocean of 3.2 S/m. The conductivity of 0.02 S/m was assigned to the subsurface.

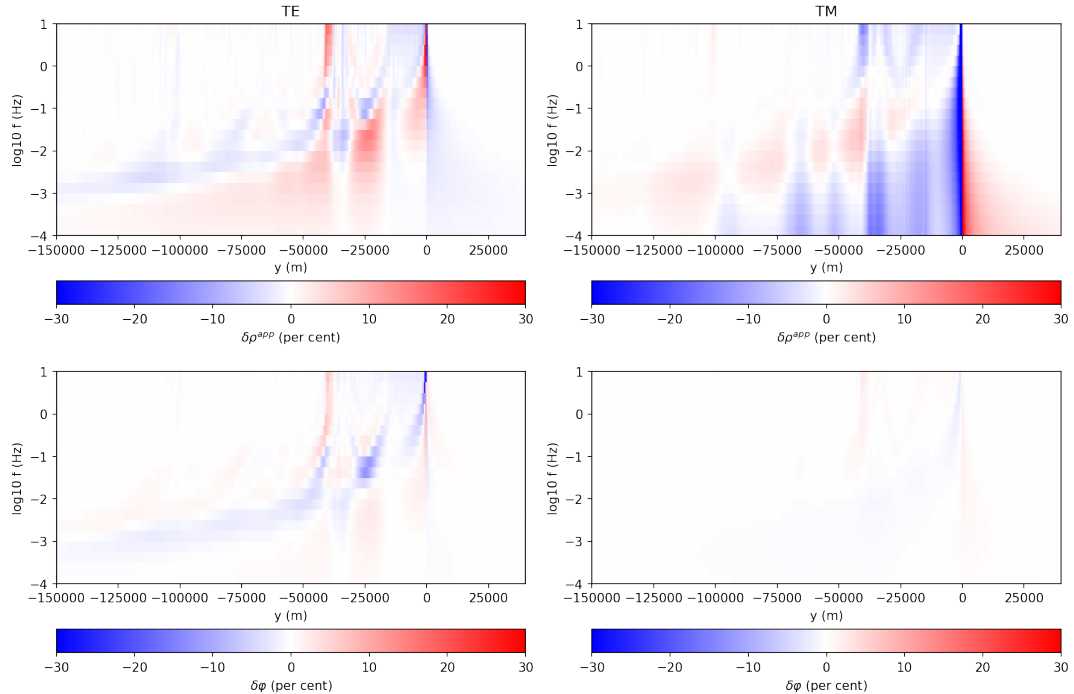


Figure 17. Same as Figure 16, but for a homogeneous subsurface conductivity of 0.1 S/m.

373 sediments exceeds that of the ocean in some regions (see Figure 7). Despite this, there
 374 is hardly any land-based MT study that elaborates on incorporation of marine sediments
 375 in the modelling. The goal of this section is to quantify the effect of marine sediments
 376 on land-based measurements and discuss implications for both inversion and space weather
 377 modelling.

378 Although there are many regions where effect of marine sediments on land EM data
 379 can be significant, we will focus on North America in this section. The reason for this
 380 choice is twofold. First, very thick sediments exist along the east coast of US that are
 381 relatively accurately mapped (Straume et al., 2019). According to the GlobSed model,
 382 the thickness of sediments on the East coast (including Gulf of Mexico) reaches 10 km,
 383 whereas it generally does not exceed 1 km along the West coast. Additionally, North Amer-
 384 ica (primarily mainland US) receives a lot of attention within the geomagnetic commu-
 385 nity due to existence of the continent-scale USAArray MT survey, which has been used
 386 for both subsurface conductivity imaging (Meqbel et al., 2014; Yang et al., 2015; Mur-
 387 phy & Egbert, 2017) and space weather hazard evaluation (Kelbert et al., 2019).

388 To assess the effect of marine sediments on land-based MT measurements, we will
 389 calculate the 3-D MT impedance tensor for models with and without sediments for North
 390 America. The conductivity model was built based on the values shown in Figure 7. Ex-
 391 cept the heterogeneous ocean and sediment layers, the subsurface was assigned a con-
 392 stant conductivity value of 0.01 S/m. This value was used as an initial model in several
 393 studies that inverted USAArray data (Meqbel et al., 2014; Yang et al., 2015). Another study
 394 by Murphy and Egbert (2017) used a close value of 0.0056 S/m. The air was assigned
 395 the conductivity of 10^{-7} S/m. Given the large extent of the model, impedance tensor
 396 transfer functions were calculated in the spherical frame following the approach of Grayver
 397 et al. (2019) to avoid artifacts due to a geographic projection and other flattening effects.

398 Figure 18 shows values of apparent resistivity and phase derived from 3-D MT impedance
 399 tensors that were calculated at the period of 11,915 s (one of the periods in the USAr-
 400 ray MT data set (Kelbert et al., 2011)) over the continent. Further, Figure 19 shows dif-
 401 ferences between models with and without marine sediments for the off-diagonal impedance
 402 tensor components (the differences for diagonal elements are not shown, but as expected
 403 they are much larger). It is evident that a significant part of what is typically referred
 404 to as “coast effect” is due to the marine sediments. The effect is much stronger along
 405 the east coast because of much thicker sediments. One sees that both apparent resistiv-
 406 ity and phases are affected. For instance, phase differences as large as 20° are observed
 407 in off-diagonal components. Compare this to a typically used 5% error floor on the impedance,
 408 which is equivalent to the 2.86° absolute phase error. Relative to this, there is a signif-
 409 icant, above the “error floor” threshold, effect of marine sediments in MT responses that
 410 penetrates hundreds of kilometres inland.

411 Next, we look how the effect of marine sediments may affect existing stations. Fig-
 412 ure 20 shows transfer functions calculated at the locations of the station FL022, mea-
 413 sured by the USGS within the GEOMAG project (Bedrosian et al., 2011). It is appar-
 414 ent here that marine sediments exhibit the first-order effect on the data. The effect is
 415 stronger in the YX component compared to the XY component since the former involves
 416 the East-West polarized electric field, which is more affected by a large conductivity gra-
 417 dient due to marine sediments.

418 There are several implications of these findings for practical studies. In subsurface
 419 conductivity imaging, one may argue that inversion should be able to compensate for
 420 the marine sediments if we give it enough degrees of freedom. However, the sensitivity
 421 to the marine sediments is only peripheral since they are outside the survey. Given the
 422 diffusive nature of the governing differential operator, typically sparse station coverage,
 423 and inherent non-uniqueness of an inverse problem, it is likely that, if not accounted for
 424 in a prior model, the inversion will compensate for marine sediments through introduc-

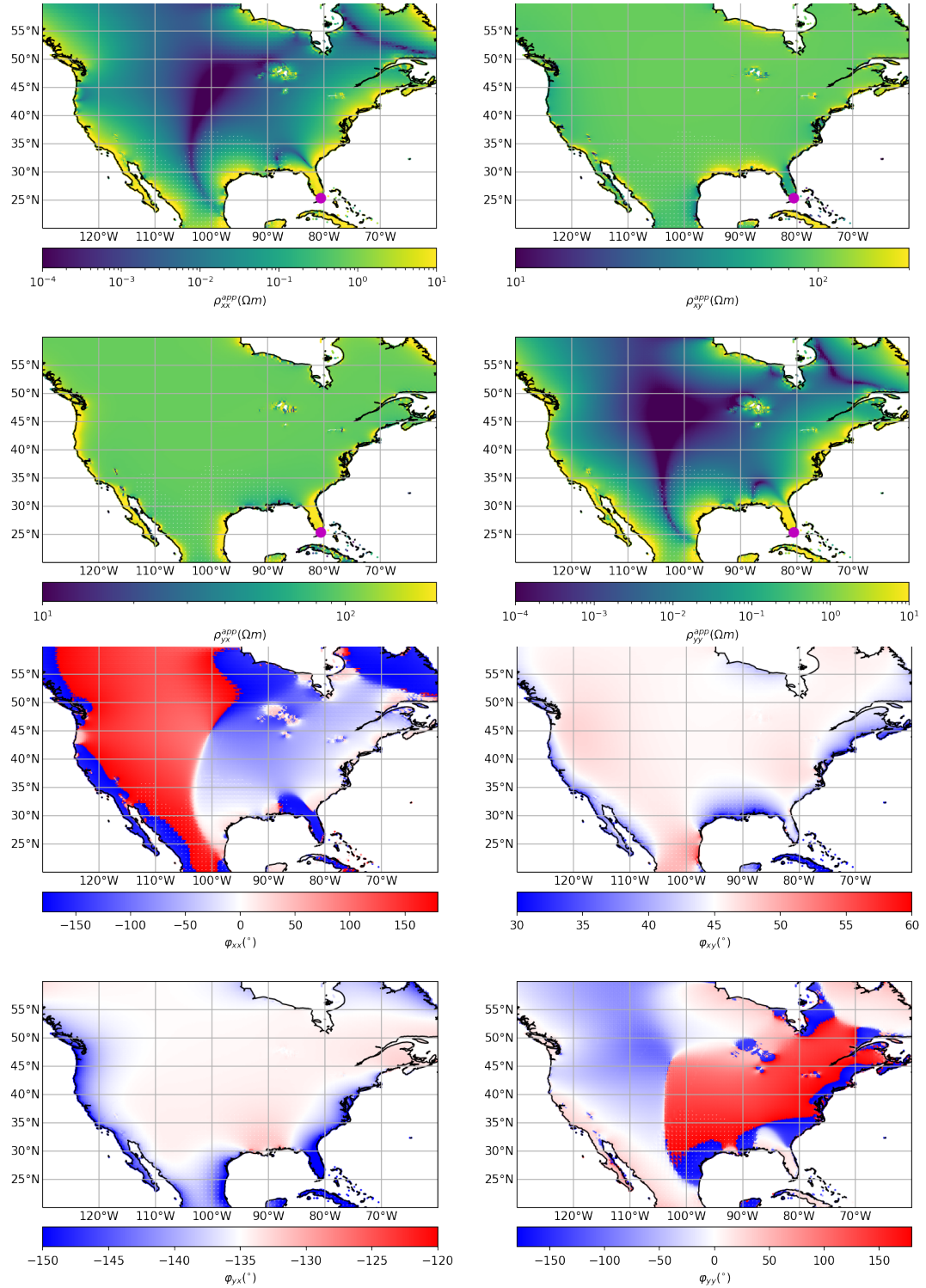


Figure 18. Distribution of the apparent resistivity and phase values over the North America continent. All four components of the impedance tensor were calculated for the period of 11,915 s. Magenta point at the southern tip of the Florida peninsula depicts the location of the FL022 station (Figure 20).

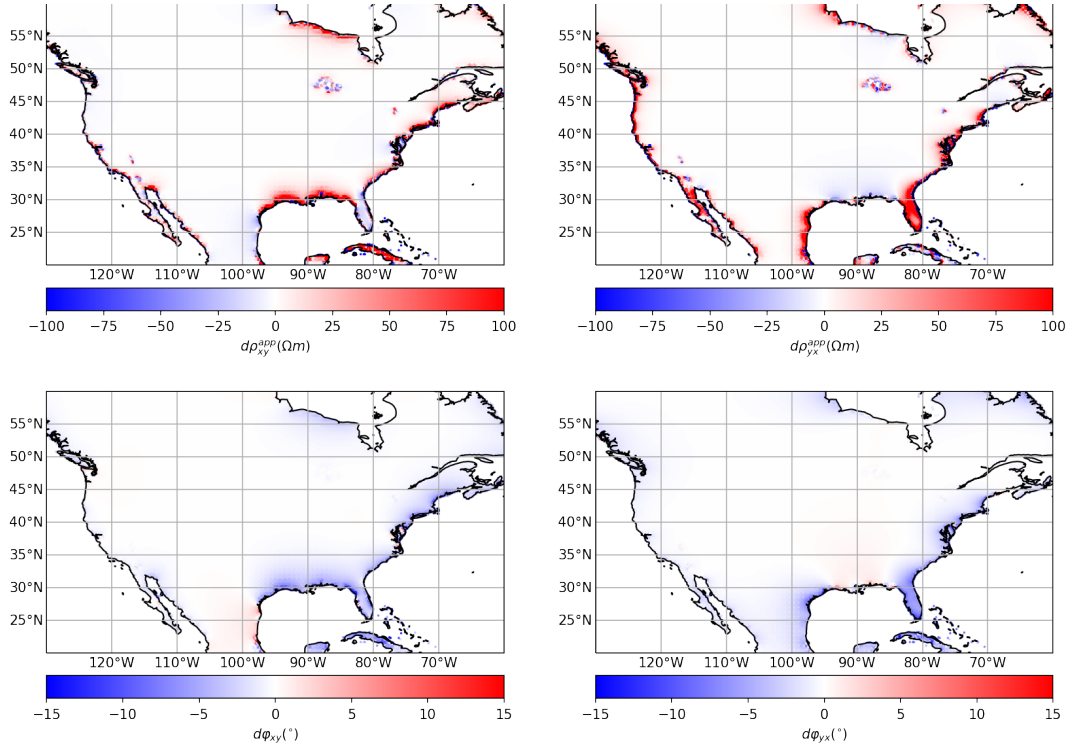


Figure 19. Differences between the diagonal components of the transfer functions calculated for models with and without marine sediments. For reference, the transfer functions for the model with marine sediments are shown in Figure 18.

tion of smooth and smeared conductive anomalies, which are likely to penetrate down to crustal depths and may lead to misinterpretations. For the space weather studies, accurate conductivity map is important in order to correctly model and asses the amplitude of GICs since conductivity contrasts generally lead to local enhancements in magnitude of GICs (Kelbert & Lucas, 2020; Marshalko et al., 2020).

5 Discussion and Conclusions

Accurate modelling of the EM induction effect due to ocean and marine sediments requires both advanced numerical methods and detailed knowledge about bathymetry, sediment thickness and, as this study demonstrated, variability of electrical conductivity within these layers. The goal of this study was to use latest data and bring this information in a form that facilitates more accurate modeling and data interpretation in EM induction and space weather studies at various scales.

A new atlas of 3-D electrical conductivity of the world ocean was created. To achieve the best resolution, it combines both global and high-resolution regional ocean climatologies derived from the World Ocean Database. The electrical conductivities were obtained by invoking the equation of state of seawater. Additionally, this work presented the first global 3-D electrical conductivity model of marine sediments. The model was constructed taking into account variable porosity and thermal gradient in the sediments. To this end, compaction and thermal models constrained by drilling and heat-flow data were used.

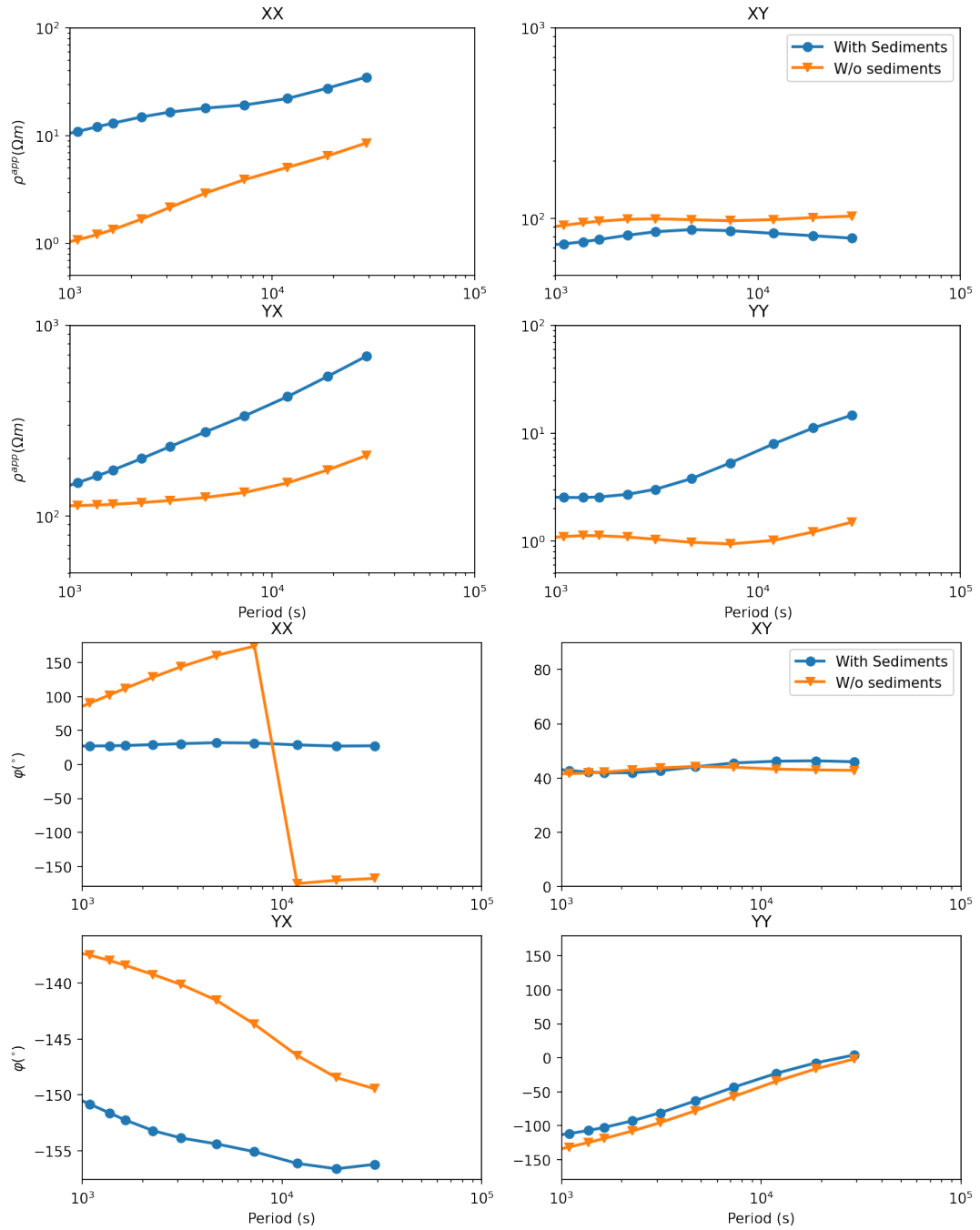


Figure 20. Apparent resistivity and phase curves calculated at the FL022 station (see Figure 18 for the exact location) using models with and without marine sediments.

Numerical experiments demonstrate that effects due to variations in electrical conductivity within the ocean and sediments are significant and sometimes have the first order impact on EM responses. Practical studies that neglect this complexity are likely to suffer from convergence problems and/or model artifacts. Despite an additional effort required to incorporate this information into the modelling, it will benefit most practical studies that deal with the modelling of EM field in presence of the ocean.

Nonetheless, it is worth to reiterate and discuss underlying assumptions and potential limitations of the models constructed here. Several variables that went into construction of the conductivity models are based on observations and have undergone some processing. Thus, there is some uncertainty that has inevitably propagated into the derived conductivity models. Some variables, such as temperature and salinity taken from the WOA18, are provided along with standard deviations. Other input data, including sediment thickness and heat flow, are not equipped with uncertainty. Additionally, we defined three types of seabed sediments based on the bathymetry. Although this approach serves as a first-order approximation and can be found in literature, in reality the diversity of seabed rocks is larger and thus their properties will vary throughout seabed. Another assumption is that the pore fluid within sediments is seawater. While the majority of pore fluid in marine sediments is seawater, it may undergo compositional alterations due to local presence of freshwater or saline brines.

In summary, while the reality is undoubtedly more complicated, models presented here aim at capturing the first-order behaviour. They also represent a significant step forward compared to currently adopted approximations. It is expected that the models published along with this study will be incrementally updated upon availability of new data.

Acknowledgments

All the World Ocean Atlas Climatology data sets are available from the NOAA WOA website. The GlobSed grid can be obtained from <https://www.ngdc.noaa.gov/mgg/sedthick/>. ETOPO1 data was retrieved from <https://www.ngdc.noaa.gov/mgg/global/>. Heat flow model was obtained from the corresponding paper cited in the text. Conductivity and conductance grids shown in this study are available at XXX. Latest updates and extra tools can also be retrieved from <https://github.com/agrayver/seasigma>. The author acknowledges support from the Swarm DISC program, funded by ESA contract no. 4000109587, with support from EO Science for Society program. This manuscript has improved through thoughtful and constructive comments by Eric Attias and an anonymous reviewer.

References

- Alekseev, D., Kuvshinov, A., & Palshin, N. (2015). Compilation of 3D global conductivity model of the Earth for space weather applications. *Earth, Planets and Space*, 67(1), 108.
- Amante, C., & Eakins, B. W. (2009). ETOPO1 arc-minute global relief model: procedures, data sources and analysis.
- Archie, G. (1942). The electrical resistivity log as an aid in determining some reservoir characteristics. *Transactions of the AIME*, 146(01), 54–62.
- Attias, E., Constable, S., Sherman, D., Ismail, K., Shuler, C., & Dulai, H. (2021). Marine electromagnetic imaging and volumetric estimation of freshwater plumes offshore hawai'i. *Geophysical Research Letters*, 48(7), e2020GL091249.
- Baba, K., Utada, H., Goto, T.-n., Kasaya, T., Shimizu, H., & Tada, N. (2010). Electrical conductivity imaging of the philippine sea upper mantle using seafloor magnetotelluric data. *Physics of the Earth and Planetary Interiors*, 183(1-2), 44–62.

- 495 Bahr, D. B., Hutton, E. W., Syvitski, J. P., & Pratson, L. F. (2001). Exponential
496 approximations to compacted sediment porosity profiles. *Computers & Geo-*
497 *sciences*, 27(6), 691–700.
- 498 Bedrosian, P. A., Kelbert, A., Burton, B. L., Morris, J. R., & Blum, C. (2011).
499 *Long-period magnetotelluric transfer functions from the florida peninsula.*
500 EMTF. doi: 10.17611/DP/EMTF/USGS/GEO MAG/FL15
- 501 Berdichevsky, M. N., & Dmitriev, V. I. (2008). *Models and methods of magnetotel-*
502 *lurics*. Springer Science & Business Media.
- 503 Boyer, T., Biddle, M., Hamilton, M., Mishonov, A., Paver, C. R., Seidov, D., &
504 Zweng, M. (2011). *Gulf of Mexico Regional Climatology* (Tech. Rep.). Regional
505 Climatology Team, NOAA/NCEI. doi: 10.7289/V5C53HSW
- 506 Boyer, T. P., Antonov, J. I., Baranova, O. K., Garcia, H. E., Johnson, D. R., Mis-
507 honov, A. V., ... others (2013). World Ocean Database 2013.
- 508 Breitzke, M. (2006). Physical properties of marine sediments. In *Marine geochem-*
509 *istry* (pp. 27–71). Springer.
- 510 Chave, A. D., & Luther, D. S. (1990). Low-frequency, motionally induced electro-
511 magnetic fields in the ocean. 1. Theory. *Journal of Geophysical Research*, 95,
512 7185–7200.
- 513 Evans, R. L. (1994). Constraints on the large-scale porosity and permeability struc-
514 ture of young oceanic crust from velocity and resistivity data. *Geophysical*
515 *Journal International*, 119(3), 869–879.
- 516 Everett, M. E., Constable, S., & Constable, C. G. (2003). Effects of near-surface
517 conductance on global satellite induction responses. *Geophysical Journal Inter-*
518 *national*, 153(1), 277–286.
- 519 Feistel, R. (2008). A gibbs function for seawater thermodynamics for- 6 to 80 c and
520 salinity up to 120 g kg⁻¹. *Deep Sea Research Part I: Oceanographic Research*
521 *Papers*, 55(12), 1639–1671.
- 522 Glover, P. W. (2016). Archie’s law—a reappraisal. *Solid Earth*, 7(4), 1157–1169.
- 523 Grayver, A. V., & Kolev, T. V. (2015). Large-scale 3d geoelectromagnetic model-
524 ing using parallel adaptive high-order finite element methodem modeling with
525 high-order fem. *Geophysics*, 80(6), E277–E291.
- 526 Grayver, A. V., Munch, F. D., Kuvshinov, A. V., Khan, A., Sabaka, T. J., &
527 Tøffner-Clausen, L. (2017). Joint inversion of satellite-detected tidal and
528 magnetospheric signals constrains electrical conductivity and water content of
529 the upper mantle and transition zone. *Geophysical research letters*, 44(12),
530 6074–6081.
- 531 Grayver, A. V., Schnepf, N. R., Kuvshinov, A. V., Sabaka, T. J., Manoj, C., &
532 Olsen, N. (2016). Satellite tidal magnetic signals constrain oceanic lithosphere-
533 asthenosphere boundary. *Science advances*, 2(9), e1600798.
- 534 Grayver, A. V., van Driel, M., & Kuvshinov, A. V. (2019). Three-dimensional mag-
535 netotelluric modelling in spherical earth. *Geophysical Journal International*,
536 217(1), 532–557.
- 537 Grevemeyer, I., & Villinger, H. (2001). Gas hydrate stability and the assessment
538 of heat flow through continental margins. *Geophysical Journal International*,
539 145(3), 647–660.
- 540 Guo, H., & Keppler, H. (2019). Electrical conductivity of nacl-bearing aqueous flu-
541 ides to 900 c and 5 gpa. *Journal of Geophysical Research: Solid Earth*, 124(2),
542 1397–1411.
- 543 Hantschel, T., & Kauerauf, A. I. (2009). *Fundamentals of basin and petroleum sys-*
544 *tems modeling*. Springer Science & Business Media.
- 545 Heinson, G., & Constable, S. (1992). The electrical conductivity of the oceanic up-
546 per mantle. *Geophysical Journal International*, 110(1), 159–179.
- 547 Jackson, P., Smith, D. T., & Stanford, P. (1978). Resistivity-porosity-particle shape
548 relationships for marine sands. *Geophysics*, 43(6), 1250–1268.

- 549 Johnson, D., & Boyer, T. P. (2015). *East Asian Seas Regional Climatology* (Tech.
 550 Rep.). NOAA/NCEI. doi: 10.7289/V5MP5171
- 551 Kelbert, A. (2020). The role of global/regional earth conductivity models in natural
 552 geomagnetic hazard mitigation. *Surveys in Geophysics*, 41(1), 115–166.
- 553 Kelbert, A., Bedrosian, P. A., & Murphy, B. S. (2019). The first 3d conductivity
 554 model of the contiguous united states: Reflections on geologic structure and
 555 application to induction hazards. *Geomagnetically induced currents from the
 556 Sun to the power grid*, 127–151.
- 557 Kelbert, A., Egbert, G., & Schultz, A. (2011). *Iris dmc data services products: Emtf,
 558 the magnetotelluric transfer functions*. EMTF. doi: 10.17611/DP
- 559 Kelbert, A., Kuvshinov, A., Velímský, J., Koyama, T., Ribaudo, J., Sun, J., ...
 560 Weiss, C. J. (2014). Global 3-D electromagnetic forward modelling: a bench-
 561 mark study. *Geophysical Journal International*, 197(2), 785–814.
- 562 Kelbert, A., & Lucas, G. M. (2020). Modified gic estimation using 3-d earth conduc-
 563 tivity. *Space Weather*, 18(8), e2020SW002467.
- 564 Key, K. (2009). 1D inversion of multicomponent, multifrequency marine CSEM
 565 data: Methodology and synthetic studies for resolving thin resistive layers.
 566 *Geophysics*, 74(2), F9–F20.
- 567 Key, K., & Constable, S. (2011). Coast effect distortion of marine magnetotelluric
 568 data: Insights from a pilot study offshore northeastern Japan. *Physics of the
 569 Earth and Planetary Interiors*, 184(3), 194–207. Retrieved from <https://www.sciencedirect.com/science/article/pii/S0031920110002487> doi:
 570 <https://doi.org/10.1016/j.pepi.2010.11.008>
- 571 Kuvshinov, A. (2008). 3-d global induction in the oceans and solid earth: recent
 572 progress in modeling magnetic and electric fields from sources of magneto-
 573 spheric, ionospheric and oceanic origin. *Surveys in Geophysics*, 29(2), 139–
 574 186.
- 575 Kuvshinov, A. (2012). Deep electromagnetic studies from land, sea, and space:
 576 progress status in the past 10 years. *Surveys in Geophysics*, 33(1), 169–209.
- 577 LaRowe, D. E., Burwicz, E., Arndt, S., Dale, A. W., & Amend, J. P. (2017). Tem-
 578 perature and volume of global marine sediments. *Geology*, 45(3), 275–278.
- 579 Larsen, J. (1968). Electric and magnetic fields induced by deep sea tides. *Geophysi-
 580 cal Journal of the Royal Astronomical Society*, 16(1), 47–70.
- 581 Laske, G. (1997). A global digital map of sediment thickness. *Eos Trans. AGU*, 78,
 582 F483.
- 583 Locarnini, R. A., Mishonov, A. V., Antonov, J. I., Boyer, T. P., Garcia, H. E., Bara-
 584 nova, O. K., ... Seidov, D. (2013). *World Ocean Atlas 2018, Volume 1:
 585 Temperature* (Tech. Rep.). NOAA Atlas NESDIS 73.
- 586 Locarnini, R. A., Mishonov, A. V., Baranova, O. K., Boyer, T. P., Zweng, M. M.,
 587 Garcia, H. E., ... Smolyar, I. (2018). *World Ocean Atlas 2018, Volume 1:
 588 Temperature* (Tech. Rep.). NOAA Atlas NESDIS 81.
- 589 Lucaeau, F. (2019). Analysis and mapping of an updated terrestrial heat flow data
 590 set. *Geochemistry, Geophysics, Geosystems*, 20(8), 4001–4024.
- 591 Manoj, C., Kuvshinov, A., Maus, S., & Lühr, H. (2006). Ocean circulation generated
 592 magnetic signals. *Earth, Planets and Space*, 58(4), 429–437.
- 593 Marshalko, E., Kruglyakov, M., Kuvshinov, A., Murphy, B. S., Rastatter, L., Ng-
 594 wira, C., & Pulkkinen, A. (2020). Exploring the influence of lateral conduc-
 595 tivity contrasts on the storm time behavior of the ground electric field in the
 596 eastern united states. *Space Weather*, 18(3), e2019SW002216.
- 597 Martin, K., & Wood, W. (2017). A new model of marine sediment compression.
 598 *Earth and Planetary Science Letters*, 477, 21–26.
- 599 McDougall, T. J., & Barker, P. M. (2011). Getting started with teos-10 and the
 600 gibbs seawater (gsw) oceanographic toolbox. *SCOR/IAPSO WG*, 127, 1–28.
- 601 Meqbel, N. M., Egbert, G. D., Wannamaker, P. E., Kelbert, A., & Schultz, A.
 602 (2014). Deep electrical resistivity structure of the northwestern us derived

- from 3-d inversion of usarray magnetotelluric data. *Earth and Planetary Science Letters*, 402, 290–304.
- Millero, F. J. (2010). History of the equation of state of seawater. *Oceanography*, 23(3), 18–33.
- Minami, T. (2017). Motional induction by tsunamis and ocean tides: 10 years of progress. *Surveys in Geophysics*, 38(5), 1097–1132.
- Murphy, B. S., & Egbert, G. D. (2017). Electrical conductivity structure of southeastern north america: Implications for lithospheric architecture and appalachian topographic rejuvenation. *Earth and Planetary Science Letters*, 462, 66–75.
- Olsen, N., & Kuvshinov, A. (2004). Modeling the ocean effect of geomagnetic storms. *Earth, planets and space*, 56(5), 525–530.
- Parkinson, W., & Jones, F. (1979). The geomagnetic coast effect. *Reviews of Geophysics*, 17(8), 1999–2015.
- Reagan, J., Zweng, M., Seidov, D., Boyer, T., Locarnini, R., Mishonov, A., ... Tyler, R. (2019). *World Ocean Atlas 2018, Volume 6: Conductivity* (Tech. Rep.). NOAA Atlas NESDIS 86.
- Revil, A., Grauls, D., & Brévart, O. (2002). Mechanical compaction of sand/clay mixtures. *Journal of Geophysical Research: Solid Earth*, 107(B11), ECV–11.
- Saynisch, J., Petereit, J., Irrgang, C., & Thomas, M. (2017). Impact of oceanic warming on electromagnetic oceanic tidal signals: A CMIP5 climate model-based sensitivity study. *Geophysical Research Letters*, 44(10), 4994–5000.
- Seidov, D., Baranova, O., Boyer, T., Cross, S., Mishonov, A., Parsons, A., ... Weathers, K. (2018). *Greenland-Iceland-Norwegian Seas Regional Climatology* (Tech. Rep.). Regional Climatology Team, NOAA/NCEI. doi: 10.7289/V5GT5K30
- Seidov, D., Baranova, O., Boyer, T., Cross, S., Mishonov, A., Parsons, A., ... Weathers, K. (2019). *Southwest North Atlantic Regional Climatology* (Tech. Rep.). Regional Climatology Team, NOAA/NCEI. doi: 10.25921/s3ag-2p18
- Seidov, D., Baranova, O., Boyer, T., Cross, S. L., Mishonov, A., & Parsons, A. (2017). *Northeast Pacific Regional Climatology* (Tech. Rep.). Regional Climatology Team, NOAA/NCEI. doi: 10.7289/V5NC5ZDN
- Seidov, D., Baranova, O., Johnson, D., Boyer, T., Mishonov, A., & Parsons, A. (2016). *Northwest Atlantic Regional Climatology* (Tech. Rep.). Regional Climatology Team, NOAA/NCEI. doi: 10.7289/V5RF5S2Q
- Seidov, D., Baranova, O. K., Boyer, T. P., Mishonov, A. V., & Parsons, A. R. (2016). *Northern North Pacific Regional Climatology* (Tech. Rep.). Regional Climatology Team, NOAA/NCEI. doi: 10.7289/v5kk98tq
- Sinmyo, R., & Keppler, H. (2017). Electrical conductivity of nacl-bearing aqueous fluids to 600 c and 1 gpa. *Contributions to Mineralogy and Petrology*, 172(1), 1–12.
- Straume, E. O., Gaina, C., Medvedev, S., Hochmuth, K., Gohl, K., Whittaker, J. M., ... Hopper, J. R. (2019). Globsed: Updated total sediment thickness in the world's oceans. *Geochemistry, Geophysics, Geosystems*, 20(4), 1756–1772.
- Trossman, D., & Tyler, R. H. (2019). Predictability of ocean heat content from electrical conductance. *Journal of Geophysical Research: Oceans*, 124(1), 667–679.
- Tyler, R. H., Boyer, T. P., Minami, T., Zweng, M. M., & Reagan, J. R. (2017). Electrical conductivity of the global ocean. *Earth, Planets and Space*, 69(1), 1–10.
- Tyler, R. H., Mysak, L. A., & Oberhuber, J. M. (1997). Electromagnetic fields generated by a three dimensional global ocean circulation. *Journal of Geophysical Research*, 102(C3), 5531–5551.
- Utada, H., Koyama, T., Shimizu, H., & Chave, A. (2003). A semi-global reference model for electrical conductivity in the mid-mantle beneath the north pacific region. *Geophysical Research Letters*, 30(4).

- 659 Velde, B. (1996). Compaction trends of clay-rich deep sea sediments. *Marine Geology*, 133(3-4), 193–201.
- 660
- 661 Velímský, J., Grayver, A., Kuvshinov, A., & Šachl, L. (2018). On the modelling of
662 M2 tidal magnetic signatures: effects of physical approximations and numerical
663 resolution. *Earth, Planets and Space*, 70(1), 1–15.
- 664 Velímský, J., Šachl, L., & Martinec, Z. (2019). The global toroidal magnetic field
665 generated in the Earth’s oceans. *Earth and Planetary Science Letters*, 509,
666 47–54.
- 667 Wallmann, K., Pinero, E., Burwicz, E., Haeckel, M., Hensen, C., Dale, A., &
668 Ruepke, L. (2012). The global inventory of methane hydrate in marine sedi-
669 ments: A theoretical approach. *Energies*, 5(7), 2449–2498.
- 670 Weatherall, P., Marks, K. M., Jakobsson, M., Schmitt, T., Tani, S., Arndt, J. E., ...
671 Wigley, R. (2015). A new digital bathymetric model of the world’s oceans.
672 *Earth and Space Science*, 2(8), 331–345.
- 673 Wheelock, B., Constable, S., & Key, K. (2015). The advantages of logarithmically
674 scaled data for electromagnetic inversion. *Geophysical Journal International*,
675 201(3), 1765–1780.
- 676 Worzewski, T., Jegen, M., & Swidinsky, A. (2012). Approximations for the 2-D
677 coast effect on marine magnetotelluric data. *Geophysical Journal Interna-*
678 *tional*, 189(1), 357–368.
- 679 Yang, B., Egbert, G. D., Kelbert, A., & Meqbel, N. M. (2015). Three-dimensional
680 electrical resistivity of the north-central usa from earthscope long period mag-
681 netotelluric data. *Earth and Planetary Science Letters*, 422, 87–93.
- 682 Zweng, M. M., Reagan, J. R., Antonov, J. I., Locarnini, R., Mishonov, A., Boyer,
683 T. P., ... Biddle, M. M. (2013). *World Ocean Atlas 2018, Volume 2: Salinity*
684 (Tech. Rep.). NOAA Atlas NESDIS 74.
- 685 Zweng, M. M., Reagan, J. R., Seidov, D., Boyer, T. P., Locarnini, R. A., Garcia,
686 H. E., ... Smolyar, I. (2018). *World Ocean Atlas 2018, Volume 2: Salinity*
687 (Tech. Rep.). NOAA Atlas NESDIS 82.